Communications and High-Precision Positioning (CHP2) System: Enabling Distributed Coherence and Precise Positioning for Resource-Limited Air Transport Systems

by

Sharanya Srinivas

A Dissertation Presented in Partial Fulfillment
of the Requirements for the Degree
Doctor of Philosophy

Approved September 2020 by the
Graduate Supervisory Committee:

Daniel W. Bliss, Chair
Christ D. Richmond
Chaitali Chakrabarti
Ahmed Alkhateeb

ARIZONA STATE UNIVERSITY

December 2020

ABSTRACT

Unmanned aerial systems (UASs) have recently enabled novel applications such as passenger transport and package delivery, but are increasingly vulnerable to cyber-attack and therefore difficult to certify. Legacy systems such as GPS provide these capabilities extremely well, but are sensitive to spoofing and hijacking. An alternative intelligent transport system (ITS) was developed that provides highly secure communications, positioning, and timing synchronization services to networks of cooperative RF users, termed Communications and High-Precision Positioning (CHP2) system. This technology was implemented on consumer-off-the-shelf (COTS) hardware and it offers rapid (<100 ms) and precise (<5 cm) positioning capabilities in over-the-air experiments using flexible ground stations and UAS platforms using limited bandwidth (10 MHz). In this study, CHP2 is considered in the context of safety-critical and resource limited transport applications and urban air mobility. The two-way ranging (TWR) protocol over a joint positioning-communications waveform enables distributed coherence and time-of-flight(ToF) estimation. In a multi-antenna setup, the cross-platform ranging on participating nodes in the network translate to precise target location and orientation. In the current form, CHP2 necessitates a cooperative timing exchange at regular intervals. Dynamic resource management supports higher user densities by constantly renegotiating spectral access depending on need and opportunity. With these novel contributions to the field of integrated positioning and communications, CHP2 is a suitable candidate to provide both communications, navigation, and surveillance (CNS) and alternative positioning, navigation, and timing (APNT) services for high density safety-critical transport applications on a variety of vehicular platforms.

ACKNOWLEDGMENTS

I would like to thank Dr. Daniel W. Bliss for his expert advice and inspiration throughout this project. I am thankful for his patience in every step of the learning process. Prof. Bliss has always been a positive reinforcement I needed to drive the research further. He was supportive of the path I chose to pursue and was consistently available to steer me whenever I was lost.

I feel grateful for Dr. Chris Richmond, Dr. Chaitali Chakrabarti and Dr. Ahmed Alkhateeb for being on my Committee. Their insightful comments drive me to seek deeper understanding. I am indebted to all the professors who taught me invaluable concepts throughout my studies here at Arizona State University.

I wish to thank Dr. P.V Sridevi for showing, by example, how a disciplined academician should be. I would also like to thank my colleagues Dr. Andrew Herschfelt, Dr. Hanguang Yu, Dr. Owen Ma, Dr. Alex Chiriyath, Dr. Yu Rong, Dr. Arindam Dutta, Wylie Standage-Beier, Adarsh Venkataramani for their support.

I am grateful to my parents Padmaja Srinivas and Srinivas Kumar for their love and constant support in every endeavor. My pursuit of higher education would not have been possible without their encouragement. Thanks to my friends Vivek Singh, Chiranjeevee Mohapatra and Prasanthi Yelamarthy for believing in me when I couldn‘t.

To my family and friends.

TABLE OF CONTENTS

Page

LIST OF FIGURES vii

1 COMMUNICATIONS & HIGH-PRECISION POSITIONING SYSTEM . 1

1.1 Background 2

1.2 Advantages and Applications 4

1.3 System Requirements 5

1.4 Contributions 6

2 SYSTEM OVERVIEW 9

2.1 System Design 9

2.1.1 System Architecture 10

2.1.2 Waveform Design 11

2.2 Time-of-Arrival (ToA) Estimation 12

2.2.1 Propagation Model 12

2.2.2 Performance Bounds 13

2.2.3 Estimation Methods 16

3 TIME-OF-FLIGHT ESTIMATION 18

3.1 Prior Work and Contributions 18

3.2 Timing Exchange Model 20

3.2.1 Setup 20

3.2.2 Timing Exchange Protocol 21

3.3 Estimation Methods 22

3.3.1 Iterative Method 22

3.3.2 Optimal One-Shot Method - First Order Model 24

3.3.3 Optimal One-Shot Method - Second Order Model 26

3.3.4 Optimal One-Shot Method - Higher Order Models 27

CHAPTER Page

3.4 Simulations 28
3.5 Summary 30
4 TIME-OF-FLIGHT TRACKING 32
4.1 Prior Work and Contributions 32
4.2 Preliminaries 35
4.2.1 Extended Kalman Filter (EKF) Tracking Algorithm 35
4.2.2 Adaptive Q Estimation Algorithm 36
4.3 Tracking Methods 39
4.3.1 First Order Markov Model 39
4.3.2 Second Order Markov Model 42
4.4 Simulations 45
4.5 Summary 46
5 JOINT POSITION AND ORIENTATION TRACKING 49
5.1 Prior Work and Contributions 50
5.2 Setup 51
5.3 Joint Position and Orientation Tracking 52
5.3.1 Problem Formulation 52
5.3.2 Tracking Preliminaries 53
5.4 Simulation Results 56
5.5 Summary 58
6 DYNAMIC SPECTRUM ACCESS 61
6.1 Motivation 62
6.2 Prior Work and Contributions 64
6.3 Revisit Time Modulation 65

CHAPTER Page

6.3.1 Estimation Rate 66
6.4 Simulations 67
6.5 Summary 69
7 EXPERIMENTAL RESULTS 72
7.1 COTS Experimental Testbed 72
7.2 Cabled Tests 72
7.3 Summary 76
8 SUMMARY AND FUTURE WORK 77
8.1 Future Work 77
8.2 Summary 79
REFERENCES 82

LIST OF FIGURES

Figure Page

1.1 Example 3x4 System Configuration With A 4-Antenna UAS And A 3-Antenna Distributed Base-Station. This Configuration Forms 12 Links Between The Users, Over Which The Communications Payloads And Positioning Sequences Are Transmitted. Each User Independently Estimates The Lengths Of Each Link With A ToA-Based ToF Estimation Algorithm. 2

2.1 Example CHP2 Network Configuration Between A 4-Antenna Distributed Base Station And A 4-Antenna UAV. These Platforms Operate With Independent, Imperfect Clocks, So There Is An Unknown Time Offset Between The Two Users. Each User Estimates The ToF Between Each Transmit-Receive Antenna Pair To Estimate The Range, Velocity, And Time Offset. 10

2.2 Overview Of Interactions Between Two Users. A Master Node Schedules Transmissions Every 50 Ms. These Two Users Alternate Between Transmitting And Receiving Every 50 Ms. When A User Receives The Joint Waveform, It Estimates The ToA Of All Positioning Sequences And Decodes The Communications Payload. It Then Packages This Information And Communicates It In The Next Frame. This Transfer Of Information Drives The Timing Synchronization And ToF Estimation Algorithm. 11

Figure Page

2.3 Basic Structure Of The Joint Waveform. Communications Segments Are Depicted In Gray, And The Positioning Sequences Are Color Coded To Indicate Different Sequences. Each Positioning Sequence Is Transmitted From A Different Transmit Antenna, Labeled Tx_1 Through Tx_4. This Allows The Receiver To Unambiguously Estimate The Path Length To Each Transmit Antenna. 12

2.4 Monte-Carlo Simulated Performance Of Three Envelope Estimators (Red, Yellow, Green), A ToA Estimator With Periodic Phase Reset (Blue) And An Ideal Phase-Coherent Estimator (Purple). The Different Envelope Implementations Have Different Fundamental Resolutions, Which Limits Their Performance At High ISNR. The Phase Coherent Estimator Measures The Carrier Phase, Which Is Ambiguous Across Carrier Cycles, So This Class Of Estimator Does Not Outperform The Envelope Estimators Unless The Estimate Is Precise To Within A Carrier Cycle, Which Breaks These Ambiguities. This Transition Occurs At High ISNR (About 45 DB), At Which Point The Ideal Estimator Transitions To The More Precise CRB. 15

3.1 Example System Configuration With A Base-Station A And An Unmanned Aerial Vehicle (UAV) B. The Two Nodes Are Separated By ToF τ and T Is The Relative Clock Offset Between The Two Radios. Node B Is Moving With Velocity $\vec{v}$ And Acceleration $\vec{a}$ Along The Direction Of Black Line. As A Result Radial Velocity $\dot{\tau}$ And Acceleration $\ddot{\tau}$ Act Along The Green Dashed Line. 19

Figure Page

3.2 Timing Exchange Protocol At Node A Where Two Successive Transmissions Are Separated By Frame Length l_A And Two Frame Constitutes A Cycle Spanning A Length Of L_A. Each Packet Comprises Of Transmit And Receive Timestamps $t_{(.),Tx}$, $t_{(.),Rx}$ Which Can Be Leveraged To Realize Joint Distributed Coherence And Ranging Estimation. 23

3.3 Simulated Flight Trajectory Of User B For 60 Seconds. User A Is Stationary, Situated At The Origin. 29

3.4 True And Estimated Relative ToF And Velocity Between The Two Users. 30

3.5 True And Estimated Relative Clock Offset And Drift Of The Aerial Node With Respect To The Ground Node. 31

4.1 Simulated Flight Trajectory Of User B For 60 Seconds. User A Is Stationary, Situated At The Origin. 45

4.2 True And Estimated Relative ToF And Velocity Between The Two Users. The EKF Estimates, Indicated Here At Every Measurement Instance, The ToF Estimates Are Precise Upto 1.2 Cm. 47

4.3 True And Estimated Relative Clock Offset And Drift Of The Aerial Node With Respect To The Ground Node. The EKF Estimates, Indicated Here At Every Measurement Instance, The Clcok Offset Estimates Are Precise Upto A 0.04ns. 48

Figure Page

5.1 CHP2 Users Estimate The Distance Between Each Cross-Platform Pair Of Antennas Using A Two-Way Ranging Algorithm And Cyclic Timing Exchange. For Multi-Antenna Users, This Spatial Diversity May Be Leveraged To Estimate The Relative Position And Orientation Of Other CHP2 Users. 50

5.2 Target Antennae Locations $\mathbf{p}_j$ When The Target Location Is $\mathbf{p}$ And Orientation Is $\boldsymbol{\theta}$ Under The Assumption That The Relative Location $\boldsymbol{\pi}_j$ Of The Antennae Are Known. 54

5.3 Simulated And Estimated Flight Trajectory Of User B For 40 Seconds. User A Is Stationary, Situated At The Origin. The EKF Estimates Are Precise Upto 2 Cm. 57

5.4 Location Of Aerial Node $\mathbf{p}$ And Its Antennae $\mathbf{p}_j$ For The Entirety Of The Flight Trajectory. 58

5.5 Relative Distance Between Radios $\mathbf{g}_1$ and $\mathbf{p}_j$ for all $j \in (1, 4)$. 59

5.6 True And Estimated Position Of The Aerial Node With Respect To The Ground Node. The EKF Estimates, Indicated Here At Every Measurement Instance, Are Precise Upto 2 Cm In Every Direction. . . . 59

5.7 True And Estimated Orientation Of The Aerial Node With Respect To The Ground Node. The EKF Estimates, Indicated Here At Every Measurement Instance, Are Precise Upto 2° In Every Direction. 60

Figure Page

6.1 System Diagram Of The Constant-Information Ranging Algorithm. A Base-Station A Tracks An Aerial User B. Based On Previous Measurements, The Base Station Predicts The Position Of User B During The Next Measurement State. Depending On How Well User A Can Predict The Path Of User B, We Can Modulate How Often A Measurement Occurs To Maintain A Constant Information Rate. If The Path Is Perfectly Predictable, No Information Is Learned By Taking Additional Measurements, So We Can Divert Spectral Resources To Other Uses. 63

6.2 Updated Timing Exchange Model Including Processing Time t_p And Dynamic Revisit Time t_r. We Consider Multiple Choices For t_r And Choose The One That Most Closely Matched The Information Constraint I_{const}. This Allows The System To Modulate The Revisit Time And Dynamically Reduce Spectral Access When The Target Behaves Predictably. 66

6.3 Simulated Flight Trajectory Of User B For 60 Seconds. User A Is Stationary, Situated At The Origin. 69

6.4 True And Estimated Relative Time-Of-Flight (ToF) And Radial Velocity Between The Two Users. The EKF Estimates, Indicated Here At Every Measurement Instance, Are Precise Upto 3 Cm And 5 Cm/s Respectively. When The Target's Flight Path Diverges From Predictions (During The Curve Vs. Straight Line) The Frequency Of Measurements Increases. 70

Figure Page

6.5 True And Estimated Relative Clock Offset And Drift Between The Two Users. The EKF Estimates Are Precise Upto 0.08 Ns And 6 Ns Respectively. When The Relative Clock Behavior Diverges From The Model (During The Curve Vs. Straight Line) Measurements Occur More Often. 71

6.6 Optimal Cycle Length To Maintain A Constant Information Of 15 Bits At Each Measurement Instance. In This Example, Using CIR To Modulate The Revisit Time Reduces Spectral Usage By Over 91%. 71

7.1 COTS Experimental Hardware Mounted In An Aluminum Frame. The Amplifier And Transmit-Receive Switching Board (Left) Is Shielded With Modular Copper Plating. The RF Board (Blue, Right) Sits On Top Of The Motherboard Underneath. The Antennas (Top Left And Right) Are Mounted To Carbon Fiber Tubes Through Which RF Feeds Are Fed And Connected To The Amplifier Board. 73

7.2 ToF Estimates Minus Mean, After Applying Deterministic Estimators HTP And STP. Both The Algorithms Perform Comparably, Maintaining A Ranging Standard Deviation Of Less Than 3 Cm. 74

7.3 ToF Estimates Minus Mean, After Applying Adaptive Extended Kalman Filters (AEKF). Adjusting The Initial Q Estimate Decreases The Observed Standard Deviation But Also Increases The Settling Time. 74

7.4 ToF Estimates Minus Mean, After Applying Adaptive Unscented Kalman Filters (AUKF). Adjusting The Initial Q Estimate Decreases The Observed Standard Deviation But Also Increases The Settling Time. 75

Chapter 1

COMMUNICATIONS & HIGH-PRECISION POSITIONING SYSTEM

Modern radio systems must adapt to limited spectral access by reducing spectrum demand and increasing operational efficiency. We design and implement a hybrid communications, navigation, and surveillance (CNS) radio system, which simultaneously performs relative positioning and network communications. Participating nodes in a distributed network of base-stations and unmanned aerial systems (UASs) engage in two-way ranging (TWR) which allows simultaneous positioning and communications tasks via a single, co-use waveform. This efficiently utilizes a limited bandwidth allocation and limits spectrum demand of new entrants. The communications task enables applications such as distributed knowledge base, air traffic management (ATM), and distributed timing synchronization, while the positioning task enables applications such as collision avoidance and automated landing. CHP2 employ novel time-of-flight (ToF) estimation methods that produces high precision ($\sigma < 5$ cm) position estimates with limited bandwidth (10 MHz). The communications task provides an encrypted data link between network nodes which enables phase-accurate timing synchronization and secures the positioning system against cyberattacks such as spoofing. Multi-antenna platforms additionally enable orientation estimation and multiple-input, multiple output (MIMO) communications. We implement this system on a consumer off the shelf (COTS) experimental testbed to demonstrate the functionality of the system and verify theoretical performance limits. The experimental results demonstrate that this technology is a viable alternative positioning, navigation, and timing (APNT) system which can support increasingly dense networks and numerous applications.

1.1 Background

Increasing demand for flying ad hoc networks (FANET) applications beyond the capabilities of existing legacy radio systems burdens the already congested spectrum bands. Diminishing spectral resources and ever growing network density urge intelligent transport systems (ITS) towards spectral sharing and co-use waveforms. Such cooperative and co-design techniques help realize RF convergence [1–3] alleviate interference between competing sensing and communications functionalities.

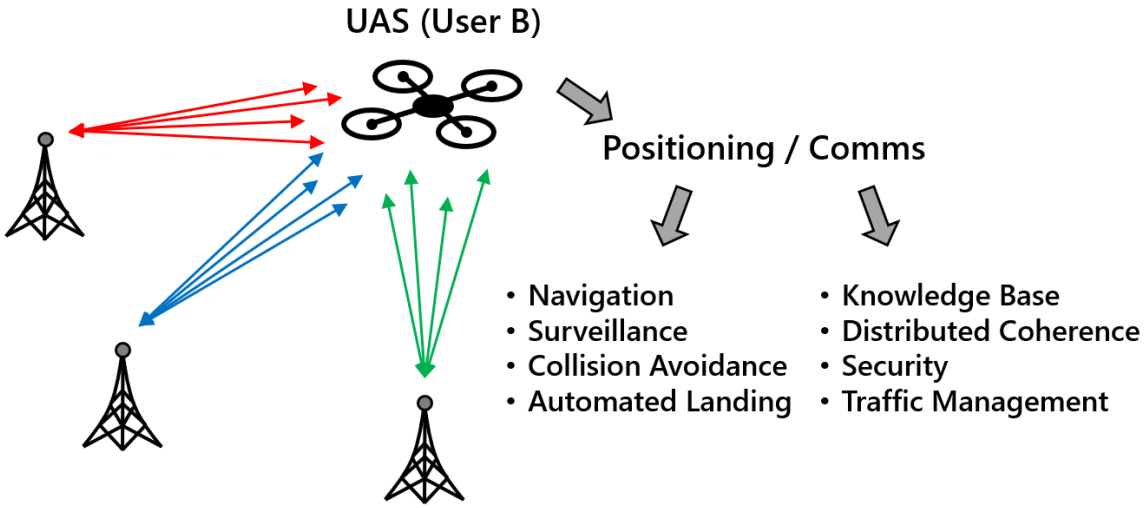

Figure 1.1: Example 3x4 System Configuration With A 4-Antenna UAS And A 3-Antenna Distributed Base-Station. This Configuration Forms 12 Links Between The Users, Over Which The Communications Payloads And Positioning Sequences Are Transmitted. Each User Independently Estimates The Lengths Of Each Link With A ToA-Based ToF Estimation Algorithm.

We design and implement an RF system that simultaneously performs positioning and communications tasks. This capability is enabled by numerous innovations, including 1) phase-coherent time-of-arrival (ToA) techniques, 2) simultaneous distributed coherence and ranging 3) joint position and orientation tracking 4) dynamic

spectral access, 5) cycle slip detection and correction etc. Previous work includes

Time-of-Flight Estimation ToF estimation algorithms use ToA estimates and information shared by the transmitter to estimate the distance between antennas and information about the clock sources. Several ToA estimators are discussed in [4] and [5] in the context of ranging. ToF has been previously considered as a localization solution [6, 7], which has recently become relatively low-cost [8]. A basic ToF algorithm is discussed in [9].

Timing Synchronization The most basic synchronization strategy is a cooperative protocol known as the network timing protocol (NTP) [10, 11]. Distributed coherent radio systems often rely on more sophisticated algorithms [12]. I explore several variants of NTP that include more parameters and higher order derivatives [4, 9] in this report.

Position Estimation Time-of-arrival (ToA) based localization of participating nodes has been studied over the past few decades [13]. In conjunction, several estimators were proposed and their performance was studied in [14], Cramér-Rao Lower Bounds (CRLB) were derived on position estimation [15] and geometric dilution of precision (GDOP) of different localization techniques was investigated in [16]; we focus on geometric interpretations of theoretical results.

Orientation Estimation Traditionally on-board inertial measurement units (IMU)s are used to determine attitude of a aerial nodes and filtering techniques are implemented to track these rotations in time [17]. Instead in this system, multi antenna radios on each node enable orientation estimation of surrounding nodes in the network purely based on the ToA estimates.

1.2 Advantages and Applications

This technology has numerous advantages over similar legacy systems. The positioning tasks achieves high precision ranging estimates ($\sigma < 5$ cm) with limited bandwidth (10 MHz) and limited acquisition time ($< 2 - 3$ s). In controlled configurations, this deviation can be driven as low as 1 mm. The joint waveform efficiently utilizes spectral resources, which supports higher user densities in network configurations and enables more tasks per bandwidth allocation. This system is implemented on COTS hardware, making it accessible, low-cost, and flexible. The small form factor allows installation on a variety of platforms, and the system does not require existing infrastructure, so it can easily be deployed in new environments without existing coverage.

This technology has numerous applications to modern vehicle systems. High-precision relative positioning enables collision avoidance, automated landing, navigation, and formation control. Secure network communications enable distributed knowledge base, real-time traffic conditions, and air traffic management. Combined, both tasks maintain distributed phase-coherence between users. The system flexibility allows quick and easy installation in areas without existing infrastructure, providing immediate coverage in situations such as disaster relief or forward operating bases. This technology further supports automation of vehicular transport by providing a cooperative medium between users, enabling vehicle-to-vehicle communications and remote control.

Precise Positioning with Limited Spectral Use

This system proved to be superior over its counterparts, for it can attain millimeter level precision ranging estimates between cross platform antennae pairs with limited bandwidth (10 MHz). These estimates can then be leveraged to acquire relative position and orientation of the neighboring nodes.

Security against spoofing

We leverage the cooperative ideology to develop joint positioning-communications system that enables distributed coherence, network communications and location sensing capabilities with limited spectral resources. Nodes in the network, communicate with single co-use waveform, over multiple antennae radios, driven by independent clocks, and are capable of precisely positioning nearby nodes. This system was implemented on consumer-off-the-shelf (COTS) radio hardware and installed on a network of base-stations and unmanned aerial vehicles (UAVs). A provision of an encrypted and dedicated communication link between participating nodes ensures security against malicious cyberattacks and protects from location errors sourced from spoofing.

Reconfigurable Design

CHP2 operates at Industrial, Scientific, and Medical (ISM) frequencies - 915 MHz in the United States or 783 MHz in Europe. Flexible design, location awareness to high precision and accessible commercial radios allows for the system to be adaptive and reconfigurable to fit a wide variety of applications, some of which are automated landing and takeoff, formation flying, collision avoidance and real-time broadcast of traffic conditions.

1.4 Contributions

The primary contributions of this report to the field of joint positioning-communications are discussed here. Firstly, I introduce the CHP2 architecture and briefly layout time-of-arrival(ToA)estimation techniques and their performance in comparison to bounds [9, 18, 19]. I propose estimation techniques that leverage ToA estimates to enable simultaneous distributed coherence and time-of-flight estimation[20]. To aid these efforts, I

- Design a family of optimal one-shot estimators that simultaneously synchronize distributed clocks and estimate relative ToF between nodes
- Identify that the delay-offset estimator reduce to a system of linear equations and is robust to inconsistencies with nodes maintaining accurate transmit instances
- Derive explicitly, estimates under the assumption that relative propagation delay and clock offset between nodes, follow first and second order Markov models
- Draw intuitions for higher order counterparts and comment on potential ambiguities

I use intuition gained from the aforementioned estimator layout to formulate a tracking algorithm that uses Kalman Filter ideology to optimally combine the measurements in time with models guided by physics [21, 22]. To aid these efforts, I

- Design a family of optimal tracking algorithms that simultaneously synchronize distributed clocks and estimate relative time-of-flight (ToF) between participating nodes using Extended Kalman filtering methodology

- Identify that the delay-offset relationship is non-linear and tailor the tracking algorithm accordingly
- Address the inconsistencies in maintaining accurate transmit instances by the participating nodes and devise algorithms that are inherently robust to such clock disparities
- Derive explicitly, necessary parameters that enable tracking under the assumption that relative propagation delay and clock offset between nodes, follow first and second order Markov models
- Draw intuitions for higher order counterparts and comment on potential ambiguities while also suggesting further improvements and identifying alternative methods.

Secondly, I propose a novel way to leverage ToF estimates from now synchronized nodes to enable joint position and orientation tracking methods using Kalman Filter ideology [23, 24]. To aid these efforts, I

- Propose a novel Extended Kalman Filter (EKF) formulation to simultaneously track position and orientation on of a target in a multi-antenna joint positioning-communications network.
- Demonstrate centimeter level positioning capabilities and orientation precise up to a few degrees.

Thirdly, I motivate the need for dynamic spectral access [25, 26]. I propose use of estimation rate as a measure of information about the target. We use this metric to optimize amount of information gained at each time instance to modulate the revisit time (time elapsed between two measurements). To aid these efforts, I

- Propose a novel, constant-information ranging algorithm that dynamically reduces spectral access by optimizing the revisit time for a moving target
- Demonstrate that the CIR algorithm significantly reduces spectral access for particular flight paths in simulation.

Lastly, I show workings of different methods previously proposed on experimental data to demonstrate that this system supports sub-cm ranging precision with 10 MHz bandwidth [27, 28].

- Compare iterative and "one-shot" techniques to Adaptive Extended Kalman filter (AEKF) and Unscented Kalman filter (UKF) tracking.

I summarize the contributions of this work to CHP2 system and identify limitations to suggest aspects that need future work.

Chapter 2

SYSTEM OVERVIEW

Unmanned aerial systems (UASs) have recently enabled novel applications such as passenger transport and package delivery, but are increasingly vulnerable to cyberattack and therefore difficult to certify. These applications require robust positioning, communications, and time synchronization services. Legacy systems such as GPS provide these capabilities extremely well, but are sensitive to spoofing and hijacking cyberattacks. In this chapter, I provide overview of a local GPS alternative that provides highly secure communications, positioning, and timing synchronization services to networks of cooperative RF users. We consider this Communications and High-Precision Positioning (CHP2) system in the context of safety-critical transport applications and urban air mobility. We discuss how the integrated communications link secures the system from spoofing and hijacking cyberattacks. We assert that the these capabilities make CHP2 a suitable candidate to provide both communications, navigation, and surveillance (CNS) and alternative positioning, navigation, and timing (APNT) services for safety-critical transport applications on a variety of vehicular platforms.

2.1 System Design

Users within this system simultaneously perform communications and positioning tasks. These tasks are performed by transmitting and receiving a co-use waveform that contains both a communications payload and several positioning reference sequences. The positioning sequences are used to estimate the ToA of the received waveform. The payload contains timing information that drives a ToF estimation

algorithm. By alternating between transmitting and receiving this information, two nodes are able to align their clocks and estimate their relative positions with high precision, see Figure 2.1. We briefly discuss the major functions of this system to motivate the experimental results.

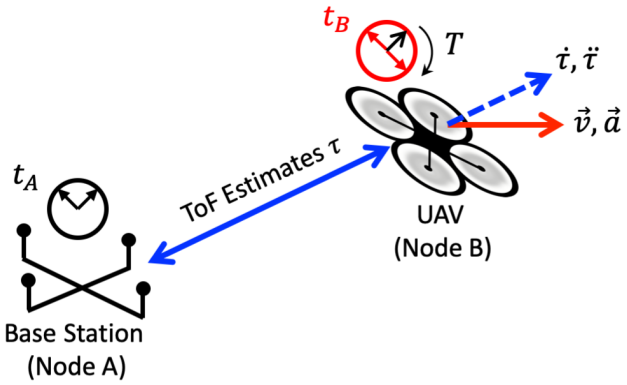

Figure 2.1: Example CHP2 Network Configuration Between A 4-Antenna Distributed Base Station And A 4-Antenna UAV. These Platforms Operate With Independent, Imperfect Clocks, So There Is An Unknown Time Offset Between The Two Users. Each User Estimates The ToF Between Each Transmit-Receive Antenna Pair To Estimate The Range, Velocity, And Time Offset.

2.1.1 System Architecture

We briefly describe the nature of the interactions between two users in this system. These two users, labeled "A" and "B", alternate between transmitting and receiving. When a user receives the joint positioning-communications waveform, it estimates the ToA of all positioning sequences on all receive channels, and extracts timing information from the communications payload. This user then assembles this information and transmits back to the other user. Transmissions are scheduled by a master node and occur every 50 ms. The joint waveform has a duration of about 1 ms. This is depicted in Figure 2.2.

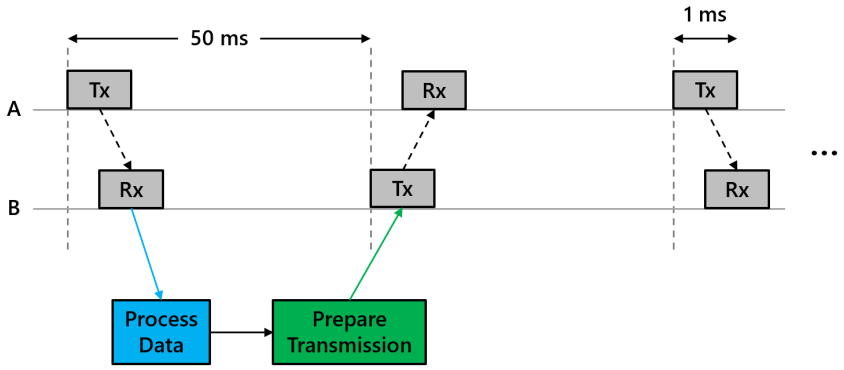

Figure 2.2: Overview Of Interactions Between Two Users. A Master Node Schedules Transmissions Every 50 Ms. These Two Users Alternate Between Transmitting And Receiving Every 50 Ms. When A User Receives The Joint Waveform, It Estimates The ToA Of All Positioning Sequences And Decodes The Communications Payload. It Then Packages This Information And Communicates It In The Next Frame. This Transfer Of Information Drives The Timing Synchronization And ToF Estimation Algorithm.

2.1.2 Waveform Design

The joint positioning-communications waveform contains a communications payload, several positioning sequences for ToA estimation, and pre- and post-ambles for acquisition and synchronization. The basic structure of the waveform is depicted in Figure 2.3 for a user with 4 antennas.

The first half of the waveform contains the communications payload and supporting amble sequences. The payload is placed between Minimum Shift Keying (MSK) pre- and post-ambles, which are used by the receiver to acquire and synchronize the received waveform. The payload is modulated using Binary Phase Shift Keying (BPSK). A second MSK post-amble is placed at the end of the waveform to enable precise frequency corrections.

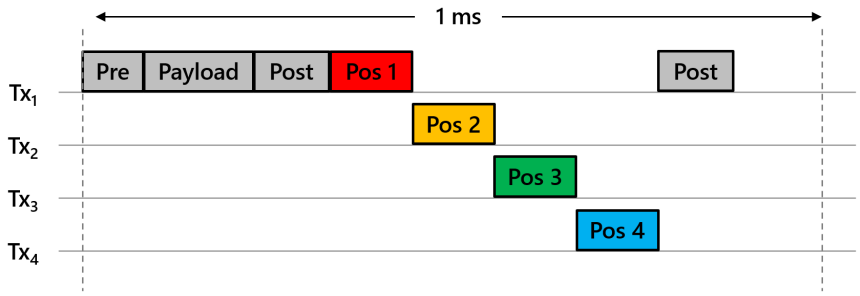

Figure 2.3: Basic Structure Of The Joint Waveform. Communications Segments Are Depicted In Gray, And The Positioning Sequences Are Color Coded To Indicate Different Sequences. Each Positioning Sequence Is Transmitted From A Different Transmit Antenna, Labeled Tx_1 Through Tx_4. This Allows The Receiver To Unambiguously Estimate The Path Length To Each Transmit Antenna.

The second half of the waveform contains the positioning sequences. These are random MSK sequences that have been treated to have low cross correlation properties with each other. One sequence is transmitted from each transmit antenna, following a Time Division Duplexing (TDD) scheme as depicted in Figure 2.3. This mitigates Inter-Symbol Interference (ISI) at the receiver, which estimates the ToA of each sequence at each receive antenna. For two 4-antenna users, there are 16 transmit-receive links that can be estimated.

2.2 Time-of-Arrival (ToA) Estimation

2.2.1 Propagation Model

We model the propagation characteristics of a signal transmitted between two nodes. Consider a complex baseband signal $x(t)$. This signal is up-converted to a carrier frequency f_c, transmitted between nodes, and down-converted at the receiver to produce a received complex baseband signal $z(t)$.

The transmitter and receiver operate with imperfect, misaligned clocks, which distorts frequency synthesis at both the transmitter and receiver. Define a misalignment factor $\zeta_{(\cdot)}$ that represents the total carrier frequency offset and whose subscript denotes which radio received the signal. A line-of-sight channel between two users A and B was modeled using these parameters in [18] as

$$z(t_B) = |a|x(t_B - t_{A,Tx}^{(n)} - \tau^{(n)} + T^{(n)})e^{jp} + n(t_B); \tag{2.1}$$

$$p = 2\pi\left(\tilde{\phi} + \zeta_B t_B - (f_{cr,n,B} + \epsilon_B + \zeta_B)\bar{\tau}_B\right), \tag{2.2}$$

where a is the complex channel attenuation, $t_{A,Tx}$ is the transmit timestamp, τ is the ToF between the platforms, T is the time offset between the clocks, t_B is the clock B time reference, n is complex additive white Gaussian noise, $\tilde{\phi}$ is phase noise induced by the hardware, channel, and miscalibration, $f_{cr,n,B}$ is the nominal clock B carrier frequency, ϵ_B is error between this nominal frequency and the actual frequency, and $\bar{\tau}_B = \tau^{(n)} - T^{(n)}$. We assume a standard LoS channel attenuation [29, 30] :

$$a^2 = \left(\frac{\lambda}{4\pi d}\right)^2 G_{Tx}G_{Rx}, \tag{2.3}$$

where G_{Tx} and G_{Rx} are the transmitter and receiver antenna gains, λ is the signal wavelength, and d is the distance between the two users.

2.2.2 Performance Bounds

The authors in [4, 5, 9, 18, 31, 32] consider two classes of ToA estimators: "envelope" and "phase-coherent".

Envelope estimators consider only the magnitude of the received signal to estimate the ToA, and are a maximization of the "incoherent" cost function

$$J_e(\tau') = \left|\int dt \;\; z(t)x^*(t-\tau')\right|^2, \tag{2.4}$$

where τ' is a delay hypothesis relative to the transmit time $t_{(\cdot),Rx}$, which is shared via the communications link. By inspection, this cost function is maximized for $\tau' \approx \tilde{\tau}$, thus define the delay estimator, and consequently the ToA estimator, as

$$\hat{t}_{e,(\cdot),Rx} = t_{(\cdot),Tx} + \hat{\tau}_e \ ; \ \hat{\tau}_e = \arg\max_{\tau'} \{J_e(\tau')\} . \tag{2.5}$$

Phase-coherent estimators consider the magnitude and phase of the received signal, and are a maximization of the "coherent" cost function

$$J_p(\tau') = \int dt \ \ z(t)x^*(t-\tau')e^{j2\pi(f_c+\hat{\zeta}_{(\cdot)})\tau'}, \tag{2.6}$$

where $\hat{\zeta}_{(\cdot)}$ is an independent estimate of $\zeta_{(\cdot)}$ generated by another mechanism. This correlation is similar to (2.4) but compensated by the expected phase shift given a delay τ'. This leverages the phase information in the received signal to potentially improve the quality of the delay estimate. The resulting estimators are likewise defined as

$$\hat{t}_{p,(\cdot),Rx} = t_{(\cdot),Tx} + \hat{\tau}_p \ ; \ \hat{\tau}_p = \arg\max_{\tau'} \{J_p(\tau')\} . \tag{2.7}$$

The Cramér-Rao Lower Bounds for (2.5) and (2.7) are well known [4] for simpler models:

$$\sigma_m^2 \leq \left(8\pi^2 \times \text{ISNR} \times B_{rms}^2\right)^{-1}, \tag{2.8}$$

$$\sigma_p^2 \leq \left(8\pi^2 \times \text{ISNR} \times \langle f_c^2 \rangle\right)^{-1}, \tag{2.9}$$

where σ^2 is the estimator variance, ISNR is the integrated SNR, B_{rms} is the RMS bandwidth, and $\langle f_c^2 \rangle$ is the mean square frequency. We simulate the performance of three envelope estimator implementations and an ideal phase-coherent estimator in Figure 2.4.

These bounds represent the best-case performance of their respective estimators. The models used to develop these estimators assume perfect synchronization between

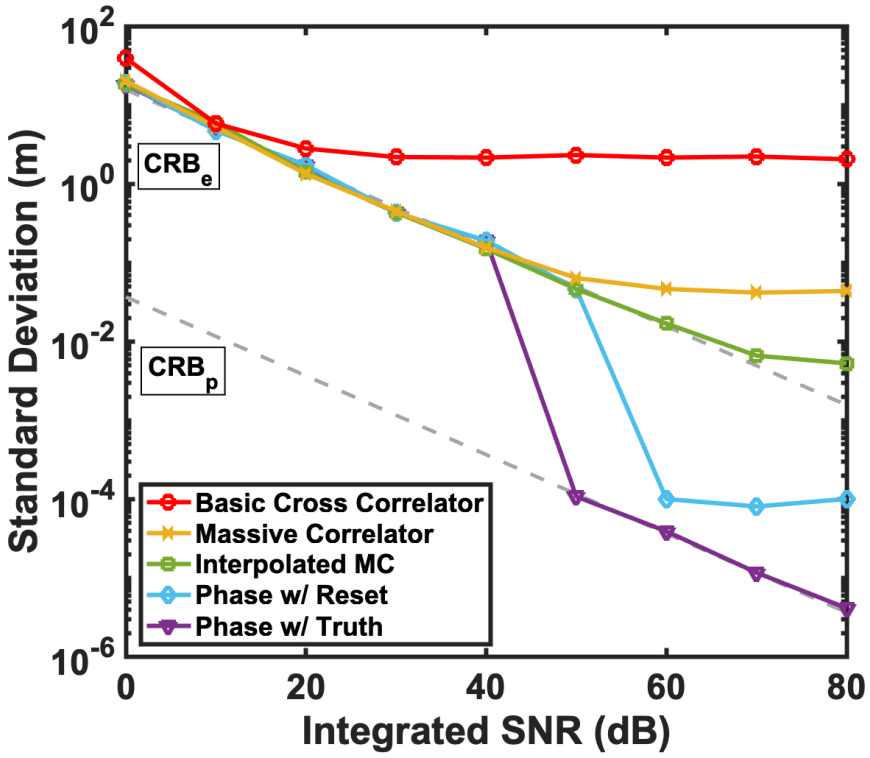

Figure 2.4: Monte-Carlo Simulated Performance Of Three Envelope Estimators (Red, Yellow, Green), A ToA Estimator With Periodic Phase Reset (Blue) And An Ideal Phase-Coherent Estimator (Purple). The Different Envelope Implementations Have Different Fundamental Resolutions, Which Limits Their Performance At High ISNR. The Phase Coherent Estimator Measures The Carrier Phase, Which Is Ambiguous Across Carrier Cycles, So This Class Of Estimator Does Not Outperform The Envelope Estimators Unless The Estimate Is Precise To Within A Carrier Cycle, Which Breaks These Ambiguities. This Transition Occurs At High ISNR (About 45 DB), At Which Point The Ideal Estimator Transitions To The More Precise CRB.

the two participating platforms; for real systems where this assumption is not realistic, "phase-coherent" estimator performance will degrade significantly. The performance penalty incurred by this model misspecification and implementation on real hardware is studied in greater detail in [4, 19].

2.2.3 Estimation Methods

Each user estimates the ToA of each positioning sequence at each receive antenna. These ToA estimates drive a ToF estimation algorithm, which then drives relative position and orientation estimators. We design a 2-stage ToA estimator that first correlates the received waveforms with a correlation bank, then refines the estimate with a 2nd order polynomial fit.

The first stage extracts the portion of the received waveform containing the target positioning sequence, and correlates it against a pre-computed bank of shifted versions of the positioning sequence. For a received signal $\mathbf{z}$ and reference sequence $\mathbf{x}$, the objective function $\mathbf{g}[k]$ measures the magnitude squared of the correlation between the two signals, indexed at discrete time shifts k. This objective function takes the form

$$\mathbf{g}[k] = \left| \sum_{m} \mathbf{z}[m]\mathbf{x}^*[m-k] \right|^2 , \tag{2.10}$$

where the summation occurs over all values of m for which the product is nonzero. The coarse ToA estimate is therefore

$$\hat{\tau} = \hat{k} f_s^{-1} \ , \ \hat{k} = \arg\max_k \mathbf{g}[k], \tag{2.11}$$

where f_s is the sampling frequency.

The correlator bank contains copies of the positioning sequence $\mathbf{x}$ shifted in time by small fractions of a sample. These sub-sample shifts are synthesized by upsampling the reference waveform, performing the shifts at the higher sampling frequency, then downsampling back to the operational sampling frequency. This enables the estimator to test hypothesizes at a higher resolution than the sampling frequency normally allows, without having to perform computations at a higher sampling frequency, which is computationally expensive.

The second stage takes several samples around the peak of the objective function $\mathbf{g}$ and applies a 2nd order polynomial fit to more accurately estimate the peak. This is implemented using a least-squares solver to estimate the coefficients of the fit in the form $y = ax^2 + bx + c$, then estimating the peak as $-b/2a$.

Chapter 3

TIME-OF-FLIGHT ESTIMATION

Limited spectral access motivates radio technologies that are capable of performing multiple tasks simultaneously and efficiently cooperating with existing systems. We develop a joint positioning-communications system for a vehicular *ad hoc* network that simultaneously synchronizes distributed users, performs carrier-phase-accurate localization, and enables network communications. In this chapter, we focus on two-way ranging methods for jointly estimating propagation delay and clock offset between the participating nodes in the network. We propose a family of novel one-shot methods [20] to achieve distributed coherence and demonstrate that, for given conditions, such estimators reduce to a system of linear equations, hence, optimal. Here, we study the precision and computational complexity of two of these estimators using simulated flight paths and discuss their region of applicability.

3.1 Prior Work and Contributions

Time-of-arrival based localization methods have been studied extensively over the past decades for line-of-sight indoor [33] and outdoor applications. Mitigation techniques have also been proposed for non line-of-sight scenarios [13]. These techniques, however, disregard clock disparities between nodes in the network. Clock synchronization [12, 34] is therefore essential for applications that rely heavily on accurate self-localization and attaining precise positioning of nearby base-stations and UAVs. Precise positioning systems rely heavily on accurate clock synchronization between the nodes. One such clock sync approach is a two way cooperative method called network timing protocol (NTP) [10, 11]. With NTP as a basis, several two-way rang-

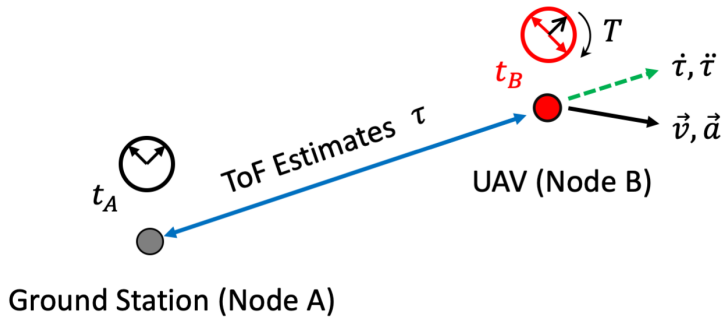

Figure 3.1: Example System Configuration With A Base-Station A And An Unmanned Aerial Vehicle (UAV) B. The Two Nodes Are Separated By ToF τ and T Is The Relative Clock Offset Between The Two Radios. Node B Is Moving With Velocity $\vec{v}$ And Acceleration $\vec{a}$ Along The Direction Of Black Line. As A Result Radial Velocity $\dot{\tau}$ And Acceleration $\ddot{\tau}$ Act Along The Green Dashed Line.

ing (TWR) methods were reported in literature [35–37]. These efforts were further extended to joint synchronization and positioning of *ad hoc* networks [5] and statistical approaches were adopted to iteratively estimate delay and clock offset parameters [38]. Such techniques, however, are limited by the following - 1) simplifying assumption on relative flight and clock parameters 2) computational complexity posed by cumbersome iterative methods, 3) lack of generality to changes in underlying models.

The joint positioning-communications system is capable of simultaneous network communications and hyper-precise localization of nodes with fewer spectral resources when compared to existing technologies, like GPS. Participating nodes operate on multi-antenna radio platforms and via two-way ranging protocol to estimate phase-accurate ToA. These estimates are then employed to jointly 1) synchronize the node and to 2) estimate ToF between cross-platform antenna pairs, which is explored in this chapter. The ToF estimates are translated to relative position and orientation estimates of the nodes. This novel algorithm specifically considers oscillators with

non-linearities while performing joint distributed coherence and positioning. The novel contributions of this chapter are

- Design a family of optimal one-shot estimators that simultaneously synchronize distributed clocks and estimate relative ToF between nodes
- Identify that the delay-offset estimator reduce to a system of linear equations and is robust to inconsistencies with nodes maintaining accurate transmit instances
- Derive explicitly, estimates under the assumption that relative propagation delay and clock offset between nodes, follow first and second order Markov models
- Draw intuitions for higher order counterparts and comment on potential ambiguities

3.2 Timing Exchange Model

3.2.1 Setup

The joint positioning-communications system supports several nodes operating over multi-antenna radio platforms and enables MIMO communications between neighboring nodes. For the sake of this discussion, however, we resort to two nodes A and B communicating over single-input-single-output (SISO) line-of-sight (LOS) environment, see Figure (3.1). Node A is a ground station and is considered stationary while node B is an unmanned aerial vehicle (UAV) moving with a velocity $\vec{v}$ and acceleration $\vec{a}$. The propagation delay for an RF waveform to traverse the distance between the two nodes is termed time-of flight (ToF) and is denoted with τ. Relative velocity and acceleration of one node with respect to the other is measured in the direction of line jointing them and is termed radial velocity ($\dot{\tau}$) and acceleration ($\ddot{\tau}$).

Nodes A and B are driven by independent clocks, which at any given time read t_A and t_B. The relative time offset (T) is the time difference between the two clocks, $T = t_A - t_B$. By convention, a positive T denotes that clock B displays an earlier time than clock A. Relative frequency offset and drift between the two clocks are represented by $\dot{T}$ and $\ddot{T}$, respectively.

3.2.2 Timing Exchange Protocol

The two radios A and B engage in a co-operative timing exchange that enables joint clock synchronization and estimation of relative positioning information. The nodes sequentially exchange timing information via the joint communications-positioning waveform, see Figure (3.2), which are then translated to corresponding timestamps using phase-accurate time-of-arrival (ToA) estimation methods. These timestamps are denoted by $t^{(.)}_{(.),(.)}$; the first subscript indicates node at which the event occurs and the second subscript indicates if it was a transmit or receive event and the superscript is an indication of frame during which the event occurs. The transmit timestamps are assumed to be known with certainty while the receive timestamps are a result of ToA estimation. Two successive frames comprise a cycle that is Ls long and is represented as $\{(n-1),(n)\}$ where the successive frames $(n-1)$ and (n) are ls apart. Despite scheduling, the nodes disagree on time hence making the cycle and frame length, dependent on the evaluating node. All essential notations are delineated in the Table (I).

During the cycle, designated master node, A transmits a packet to B in the frame $(n-1)$, B waits for an agreed frame separation l and transmits a packet to A during the next frame (n). Each packet comprises of transmit and receive timestamps $t_{(.),Tx}$, $t_{(.),Rx}$ for the previous frame along with communication payload. Through the entirety of the paper, we are concerned with estimating clock offset (T) and relative ToF (τ)

between the two nodes for the cycle containing $(n-1)^{th}$ and $(n)^{th}$ frames while making an assumption that estimates of these parameters for previous cycles are available. The same ideology can be extended to the estimate the parameters of interest for any time instance. For a transmission from A to B, during frame $(n-1)$, node B will receive the signal at time

$$t_{B,Rx}^{(n-1)} = t_{A,Tx}^{(n-1)} + \tau^{(n-1)} - T^{(n-1)}. \tag{3.1}$$

whereas a transmission from B to A, during frame (n), node A will receive the signal at time

$$t_{A,Rx}^{(n)} = t_{B,Tx}^{(n)} + \tau^{(n)} + T^{(n)}. \tag{3.2}$$

The transmit timestamp $t_{B,Tx}^{(n)}$ is perceived by node A as $\tilde{t}_{A,Tx}^{(n)}$ due to clock discrepancies, see Figure (3.2).

$$\tilde{t}_{A,Tx}^{(n)} = t_{B,Tx}^{(n)} + T^{(n)} \tag{3.3}$$

Also, frame length l measures to l_A and cycle separation L to L_A respectively on clock driving node A, which for the current cycle of interest become

$$l_A^{(n-1)} = \tilde{t}_{A,Tx}^{(n)} - t_{A,Tx}^{(n-1)}, \tag{3.4}$$

$$L_A^{(n-1)} = t_{A,Tx}^{(n-1)} - t_{A,Tx}^{(n-3)}. \tag{3.5}$$

In this report, we explore joint delay and offset tracking at node A, though an equivalent at node B is straightforward, it is out of scope for this discussion.

3.3 Estimation Methods

3.3.1 Iterative Method

We proposed an iterative ToF estimation algorithm. It is a two step process where initial coarse estimates are derived using the Network Timing Protocol (NTP)

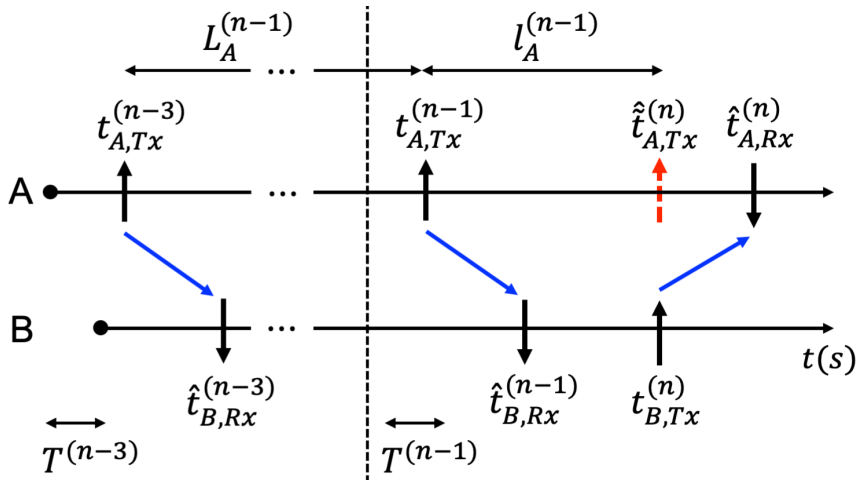

Figure 3.2: Timing Exchange Protocol At Node A Where Two Successive Transmissions Are Separated By Frame Length l_A And Two Frame Constitutes A Cycle Spanning A Length Of L_A. Each Packet Comprises Of Transmit And Receive Timestamps $t_{(.),Tx}$, $t_{(.),Rx}$ Which Can Be Leveraged To Realize Joint Distributed Coherence And Ranging Estimation.

Table 3.1: Terminology pertaining to Timing Exchange Protocol

$t_{A,Tx}, t_{B,Tx}$	Transmit and receive event time-stamps at node A
$t_{A,Rx}, t_{B,Rx}$	Transmit and receive event time-stamps at node B
$\tilde{t}_{A,Tx}$	Transmit event time-stamp $t_{B,Tx}$ at node A
l_A, L_A	Frame length and cycle length at node A
$\tau, \dot{\tau}, \ddot{\tau}$	Relative ToF, velocity and acceleration
$T, \dot{T}, \ddot{T}$	Relative time offset, frequency offset and drift

standard. These estimates are then iteratively corrected under the first order Markov model assumption to get precise ranging.

NTP assumes that the state space is constant for a duration of a cycle $\{(n -$

$1), (n)\}$. Therefore the coarse ToF estimates are reduced to

$$\tau^{(n-1)} = \tau^{(n)} = \frac{\gamma_A}{2}, \tag{3.6}$$

which are then utilized to generate initial estimates for clock offsets $T^{(n-1)}$ and $T^{(n)}$ using (3.1) and (3.2). γ_A is

$$\gamma_A = (t_{A,Rx}^{(n)} - t_{A,Tx}^{(n-1)}) - (t_{B,Tx}^{(n)} - t_{B,Rx}^{(n-1)}). \tag{3.7}$$

We now relax this assumption and employ iterative tactics to attain finer precision in ToF estimates. We introduce first order derivatives $\dot{\tau}$ and $\dot{T}$ and compensate for their effect at every iteration k with the following

$$\tau^{(k+1,n-1)} = \frac{\gamma_A - \left(\dot{\tau}^{(k,n-1)} + T^{(k,n-1)}\right) l_A^{(k,n-1)}}{2}, \tag{3.8}$$

$$\tau^{(k+1,n)} = \frac{\gamma_A + \left(\dot{\tau}^{(k,n)} - T^{(k,n)}\right) l_A^{(k,n)}}{2}, \tag{3.9}$$

until convergence. This first generation estimation method is simple but inelegant, cumbersome, and sub-optimal.

3.3.2 Optimal One-Shot Method - First Order Model

Here, we examine joint clock synchronization and relative ranging estimation between two nodes A and B under the assumption that propagation delay τ and time offset T follow first order Markov model, hence the title. We identify that the estimator reduces to *solving a system of two linear equations* under this scenario. Sufficient information is accrued only after two frames, hence parameters of interest are estimated every cycle and the results are extrapolated to each frame.

Under the 1^{st} order Markov model assumption,

$$\tau^{(n)} = \tau^{(n-1)} + \dot{\tau}^{(n-1)} l_A^{(n-1)} \tag{3.10}$$

$$T^{(n)} = T^{(n-1)} + T^{(n-1)} l_A^{(n-1)} \tag{3.11}$$

where $\dot{\tau}$ and T rely on estimates of previous transmission frame $(n-3)$ as

$$\dot{\tau}^{(n-1)} = \frac{\tau^{(n-1)} - \tau^{(n-3)}}{L_A^{(n-1)}} \tag{3.12}$$

$$T^{(n-1)} = \frac{T^{(n-1)} - T^{(n-3)}}{L_A^{(n-1)}} \tag{3.13}$$

Exploiting these postulations, equations (3.1) and (3.2) reduce to a system of linear equations in $\tau^{(n-1)}$ and $T^{(n-1)}$ as

$$\tau^{(n-1)} - T^{(n-1)} = \delta^{(n-1)} \tag{3.14}$$

$$\varepsilon^{(n-1)}\,\tau^{(n-1)} + \zeta^{(n-1)}\,T^{(n-1)} = \eta^{(n-1)} \tag{3.15}$$

where

$$\delta^{(n-1)} = t_{B,Rx}^{(n-1)} - t_{A,Tx}^{(n-1)} \tag{3.16}$$

$$\varepsilon^{(n-1)} = L_A^{(n-1)} + t_{B,Tx}^{(n)} - t_{A,Tx}^{(n-1)} + T^{(n-3)} \tag{3.17}$$

$$\zeta^{(n-1)} = L_A^{(n-1)} + t_{A,Rx}^{(n)} - t_{A,Tx}^{(n-1)} - \tau^{(n-3)} \tag{3.18}$$

$$\eta^{(n-1)} = t_{A,Rx}^{(n)}\,(\,T^{(n-3)} + L_A^{(n-1)}\,) + \tag{3.19}$$

$$t_{B,Tx}^{(n)}\,(\,\tau^{(n-3)} - L_A^{(n-1)}\,) - t_{A,Tx}^{(n-1)}\,(\,\tau^{(n-3)} + T^{(n-3)}\,)$$

and the frame length is estimated as

$$l_A^{1,(n-1)} = \frac{t_{B,Tx}^{(n)} - t_{A,Tx}^{(n-1)} + T^{(n-1)}}{1 - T^{(n-1)}} \tag{3.20}$$

The time-of-flight (ToF) and clock offset estimates, $\tau^{(n-1)}$ and $T^{(n-1)}$ at node A are obtained by solving (3.14) and (3.15) as follows

$$\tau^{(n-1)} = \frac{\eta^{(n-1)} + \zeta^{(n-1)}\delta^{(n-1)}}{\varepsilon^{(n-1)} + \zeta^{(n-1)}} \tag{3.21}$$

$$T^{(n-1)} = \frac{\eta^{(n-1)} - \varepsilon^{(n-1)}\delta^{(n-1)}}{\varepsilon^{(n-1)} + \zeta^{(n-1)}} \tag{3.22}$$

and clock frequency offset (T) and radial velocity $(\dot{\tau})$ are evaluated using (3.12) and (3.13). These estimates at frame $(n-1)$ are extrapolated to obtain $\tau^{(n)}$ and $T^{(n)}$

for $(n)^{th}$ frame, using (3.10) and (3.11), thus preserving a resolution of a frame. Since $\hat{l}_A$ is estimated in the process, the joint estimator is robust to inconsistencies in maintaining a constant frame length. It is important to identify the simplicity and optimality of this one-shot estimator compared to its iterative predecessors.

3.3.3 Optimal One-Shot Method - Second Order Model

In this section, we extend the previous formulation to include non-zero second order derivatives of offset and delay, frequency drift $\ddot{T}$ and radial acceleration $\ddot{\tau}$ respectively and derive the estimation algorithm for this renewed premise. We recognize that despite its non-linear appearance, the estimator still reduces to a system of linear equations. We address the ambiguities induced by second order formulation and computational complexity incurred in resolving them.

The 2^{nd} order Markov model construction necessitates that,

$$\tau^{(n)} = \tau^{(n-1)} + \dot{\tau}^{(n-1)} l_A^{(n-1)} + \frac{1}{2}\ddot{\tau}^{(n-1)} l_A^{(n-1)^2} \tag{3.23}$$

$$T^{(n)} = T^{(n-1)} + T^{(n-1)} l_A^{(n-1)} + \frac{1}{2}\ddot{T}^{(n-1)} l_A^{(n-1)^2} \tag{3.24}$$

where $\dot{\tau}$ and T follow (3.12), (3.13) respectively while T and $\ddot{\tau}$ are

$$\ddot{\tau}^{(n-1)} = \frac{\dot{\tau}^{(n-1)} - \dot{\tau}^{(n-3)}}{L_A^{(n-1)}} \tag{3.25}$$

$$\ddot{T}^{(n-1)} = \frac{T^{(n-1)} - T^{(n-3)}}{L_A^{(n-1)}} \tag{3.26}$$

Under these assumptions, equations (3.1) and (3.2) reduce to

$$\tau^{(n-1)} - T^{(n-1)} = \delta^{(n-1)} \tag{3.27}$$

$$\begin{aligned} &\tau^{(n-1)} + \dot{\tau}^{(n-1)} l_A^{(n-1)} + \tfrac{1}{2}\ddot{\tau}^{(n-1)} l_A^{(n-1)^2} + \\ &T^{(n-1)} + T^{(n-1)} l_A^{(n-1)} + \tfrac{1}{2}\ddot{T}^{(n-1)} l_A^{(n-1)^2} \end{aligned} = \lambda^{(n-1)} \tag{3.28}$$

where

$$\delta^{(n-1)} = t_{B,Rx}^{(n-1)} - t_{A,Tx}^{(n-1)} \tag{3.29}$$

$$\lambda^{(n-1)} = t_{A,Rx}^{(n)} - t_{B,Tx}^{(n)} \tag{3.30}$$

and $l_A^{(n-1)}$ is now evaluated by solving the following quadratic function

$$\frac{1}{2}\,\alpha^{(n-1)}\,l_A^{(n-1)^2} - \beta^{(n-1)}\,l_A^{(n-1)} + \gamma^{(n-1)} = 0 \tag{3.31}$$

where

$$\alpha^{(n-1)} = \ddot{T}^{(n-1)} \quad , \quad \beta^{(n-1)} = 1 - T^{(n-1)} \tag{3.32}$$

$$\gamma^{(n-1)} = T^{(n-1)} + t_{B,Tx}^{(n)} - t_{A,Tx}^{(n-1)} \tag{3.33}$$

This can be verified by setting $\ddot{T}^{(n-1)} = 0$ and as a consequence $l_A^{(n-1)}$ reduces to (4.22). The estimates of frame length, which exists if and only if $\hat{\beta}^{(n-1)^2} - 2\,\alpha^{(n-1)}\gamma^{(n-1)} \geq 0$, are

$$l_A^{2,(n-1)} = \frac{\beta^{(n-1)} \pm \sqrt{\hat{\beta}^{(n-1)^2} - 2\,\alpha^{(n-1)}\gamma^{(n-1)}}}{\alpha^{(n-1)}} \tag{3.34}$$

only one of which is feasible and determined by conditioning $\hat{l}_A \geq 0$. Though equations (3.27) and (3.28) seem non-linear, they are infact linear when substituted for $\hat{l}_A$ and can be validated by plotting the two equations with τ and T on X-Y axis, for any valid set of parameters in their domain. It is neither convenient nor intuitive to write out the estimates for τ and T explicitly. With assumptions delineated in (3.12), (3.13), (3.25) and (3.26), first and second order derivatives of propagation delay and clock offset are estimated which then are extrapolated to derive parameter estimates for frame (n) using (3.23) and (3.24).

3.3.4 Optimal One-Shot Method - Higher Order Models

In the previous sections, we derived the joint ranging and clock synchronization estimators for first and second order Markov models assumptions on relative delay

and offset between participating nodes. Here, we extend this ideology to generalize for higher orders and comment on potential ambiguities incurred in the estimation process. Including higher order derivatives of state space parameters helps broaden localization for complex flight maneuvers and clock inconsistencies hence increasing range of applicability for the estimators. These variations have not been explored in literature prior to this work for their perceived complexity which makes the following discovery a significant contribution to the field. We discovered that the optimal one-shot joint delay-offset estimator formulated with k^{th} order Markov model assumption minimizes to a system of linear equations, for any k. The frame length $l_A^{k,((.))}$ is estimated by solving a k^{th} order polynomial function which then induces k ambiguities. Despite the fact that solving such higher order functions and resolving ambiguities drives up computational costs, we can be assured that an optimal solution exists and is the point of intersection of two lines in delay-offset domain.

3.4 Simulations

We demonstrate that joint delay-offset estimation in the context of CHP2. We simulated a stationary, ground user A and a mobile, airborne user B following an arbitrary flight path (Figure 3.3). We study through simulations, performance of the first and second order joint delay-offset estimation methods. Following the setup provided in Figure (3.1), we simulate two nodes A and B, while A is stationary and tethered to the ground, B is airborne and flying in a three dimensional space. Both the nodes are driven by independent clocks which at any given time read t_A and t_B.

Under this scenario, the two nodes co-operatively exchange timing information every frame which are $\hat{l}_A = 50$ ms apart. The transmit timestamps $t_{A,Tx}$ and $t_{B,Tx}$ are assumed to be known with certainity and the receive timestamps $\hat{t}_{A,Rx}$ and $\hat{t}_{B,Rx}$ are a result of carrier-phase-accurate time of arrival (ToA) estimation and are known

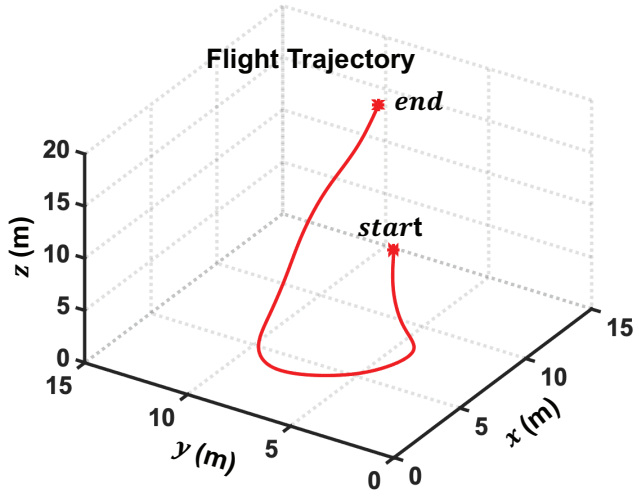

Figure 3.3: Simulated Flight Trajectory Of User B For 60 Seconds. User A Is Stationary, Situated At The Origin.

to a precision σ_{ToA}. We are interested in the regime where the SNR of the received signal in this two-way communication between participating nodes exceeds 45 dB, resulting in ToA estimates that are precise upto 3cm $\sim 1^{-10}$s

Node A is the designated master node and is tasked with estimating the relative delay ($\hat{\tau}$) and clock offset ($\hat{T}$) between the two radios. Using the timestamps $t_{A,Tx}$, $t_{B,Tx}$, $\hat{t}_{A,Rx}$ and $\hat{t}_{B,Rx}$, the parameters of interest are estimated via (a) first order joint delay-offset estimator using equations (3.21) and (3.22) and (b) second order estimator by solving for equations (3.27) and (3.28) using `vpasolve()` in MATLAB©. The estimates produced are associated with the transmit timestamps $t_{A,Tx}$, $\tilde{t}_{A,Tx}$ which in turn rely on frame length estimates.

CHP2 operates with 30 dB of waveform integration gain and maintains an operational instantaneous SNR of 15 dB, which yields ToA estimates precise to within 0.1 ns (3 cm) [9]. The one-shot optimal estimates of ToF and radial velocity are precise up to 1.2 cm and 15 cm/s, see Figure (3.4) and clock offset and drive are precise up to 0.04ns and 1.2ns, see Figure (3.5).

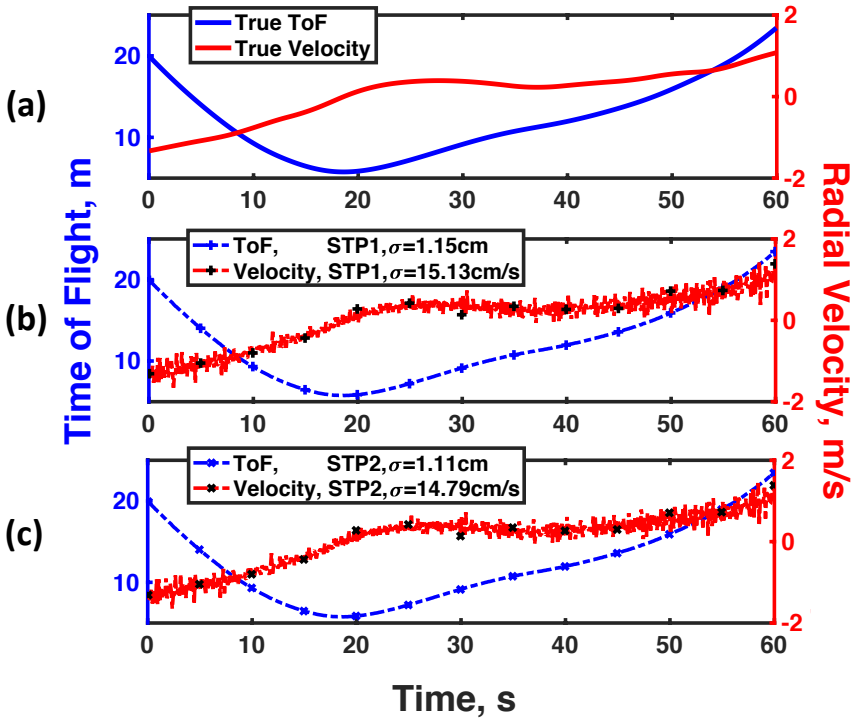

Figure 3.4: True And Estimated Relative ToF And Velocity Between The Two Users.

3.5 Summary

Localization is key for highly adaptive self-organizing *ad hoc* networks. Increasing demand and diminishing spectral resources necessitate co-designed positioning systems. We developed a joint positioning-communications system that enables network communications and precise localization with fewer spectral resources. In this chapter, we proposed a family of optimal one-shot methods that jointly achieve distributed coherence and ranging estimation. We recognize that such estimators reduce to a system of linear equations and hence are optimal. We studied through simulations, precision, computational complexity and region of applicability for two of such variants and comment on higher order generalizations.

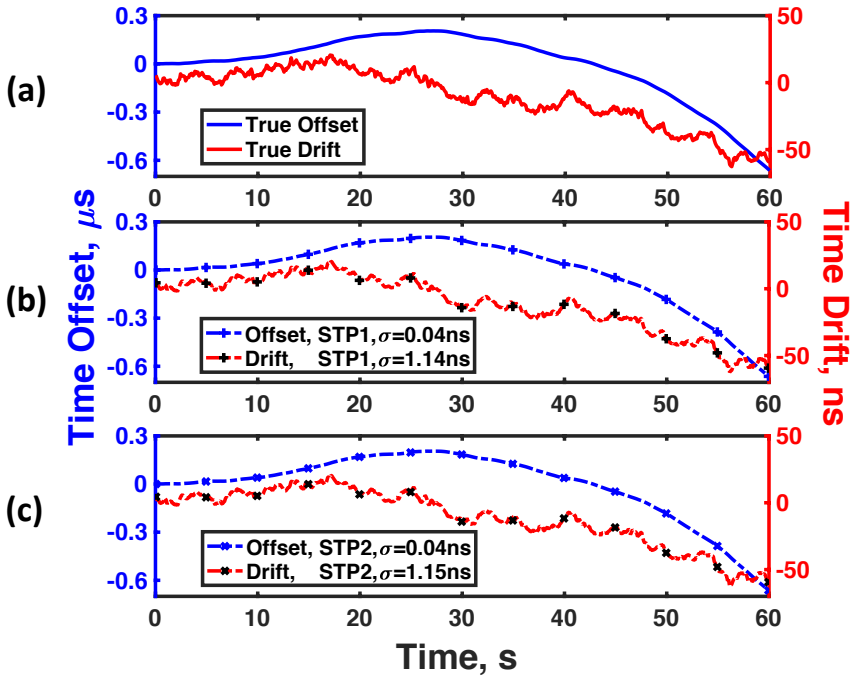

Figure 3.5: True And Estimated Relative Clock Offset And Drift Of The Aerial Node With Respect To The Ground Node.

Chapter 4

TIME-OF-FLIGHT TRACKING

In this chapter, we propose a family of novel Extended Kalman Filter (EKF) estimators that realize clock synchronization in a distributed system while simultaneously track ranging information between participating users. We focus on two of these methods which assume that the relative propagation delay and clock offset between nodes follow first and second order Markov models [21] and provide generalizations for higher order models. We study performance of the two tracking algorithms via simulated flight paths and comment on how compare against the optimal one-shot estimators.

4.1 Prior Work and Contributions

Localization is key for highly adaptive self-organizing *ad hoc* networks. An extensive review on positioning using angle-of-arrival (AoA), time-of-arrival (ToA), time difference-of-arrival (TDoA) and received-signal-strength (RSS) is presented in [33, 39–43]. Time-of-arrival based positioning methods [13] are popular among the bunch and have been a topic of interest for several decades now. Precision in ToA estimates [8] directly informs the resolution in positioning of nodes in the network and Cramér Rao lower bounds on ToA estimation have been derived [4, 31] However, often, these positioning systems disregard clock disparities which is reasonable if the setup resembles Global Positioning system (GPS) where localization is one-way and satellites have access to atomic clocks [44, 45]. However, we are interested in two-way positioning of several communicating users operating on independent clocks which in themselves are not as sophisticated.

Since precise positioning relies heavily on accurate clock synchronization [34, 46–49], coherence among distributed users in mandatory. One such approach is Network Timing Protocol (NTP) [10, 11], that leverages two-way exchange of timing information to sync clocks and has been baked into Precise Point Positioning (PPP) standard [50]. Inspired by the simplicity of NTP, several advancements were proposed in [51–55]. These efforts into accurate two-way clock sync were married with ToA timestamp based ranging estimation to devise joint systems that realize simultaneous propagation delay and clock offset estimation in [4, 5, 38]. The proposed methods were however riddled with simplifying assumptions that limit operating environments, computational complexity posed by cumbersome iterative estimators and lack of generality to changes in underlying models.

Therefore, we proposed a family of novel one-shot estimators in [20] that leverage high precision ToA estimates to simultaneously synchronize distributed clocks and estimate relative time-of-flight (ToF) between participating users. In our approach, we do not introduce any simplifying assumptions. We demonstrated that the estimators, termed Srinivas Timing Protocols [18], are optimal and reduce to a *system of linear equations*. In this journal, we take inspiration from these estimators and reformulate them to enable tracking of parameters of interest using Kalman filtering [56–58] algorithms. The information accrued, is then translated to relative location and orientation of individual nodes, but is out of scope for present discussion.

Estimating clock errors involves solving stochastic differential equations whose coefficients are derived from Allan variance[59] characteristics of oscillators that inherently drive these clocks[60]. Kalman filter based clock synchronization have been well researched topic [61, 62] and several formulations were proposed to realize such tracking of clock drifts. We draw insights provided in [63] and [64] to actualize joint distributed coherence and time-of-flight tracking using Extended Kalman Filters. We

do not consider flicker noise while modeling the clocks but interested reader are directed to [65–67] and references therein.

It is important to note that a significant issue with ToA based localization, is when operating in multipath environments where there is no direct line-of-sight (LoS) between the two communicating nodes causing huge positioning errors. We do not address these concerns but several non LoS mitigation techniques were discussed in the past and interested readers are referred to[13, 68, 69] and the references therein.

The novel contributions of this chapter to the field are as follows

- Design a family of optimal tracking algorithms that simultaneously synchronize distributed clocks and estimate relative time-of-flight (ToF) between participating nodes using Extended Kalman filtering methodology
- Identify that the delay-offset relationship is non-linear and tailor the tracking algorithm accordingly
- Address the inconsistencies in maintaining accurate transmit instances by the participating nodes and devise algorithms that are inherently robust to such clock disparities
- Derive explicitly, necessary parameters that enable tracking under the assumption that relative propagation delay and clock offset between nodes, follow first and second order Markov models
- Draw intuitions for higher order counterparts and comment on potential ambiguities while also suggesting further improvements and identifying alternative methods.

4.2 Preliminaries

4.2.1 Extended Kalman Filter (EKF) Tracking Algorithm

From earlier discussion, we deduce that timestamps from two successive frames, say $\{(n-1),(n)\}$, encompass information necessary to conduct joint estimation, see equations (3.1) and (3.2). Therefore, we employ tracking once every cycle, producing state space estimates at a resolution of cycle (= two frames). Kalman filters inherently assume Gaussian processes which non-linear problems fails to preserve. Extended Kalman Filters (EKF) [57] counter this issue by linearizing the non-linear transformations, thus preserving gaussianity. The algorithm can be visualized as a two steps - 1) Prediction and 2) Correction. State space parameters at time instance $(n-1)$ are predicted using estimates from previous cycle $\hat{\mathbf{x}}^{(n-3)}$ as,

$$\hat{\mathbf{x}}_{(-)}^{(n-1)} = \mathbf{F}\left(L_A^{(n-1)}\right)\ \hat{\mathbf{x}}^{(n-3)} + \mathbf{w}^{(n-1)} \tag{4.1}$$

where $\mathbf{F}(.)$ is the state transition, L_A is the cycle length, see equation (3.5) and $\mathbf{w}^{(.)} \sim \mathcal{N}(0, \mathbf{Q}^{(.)})$ is the process noise, assumed to be drawn from a zero-mean, multivariate normal distribution. The error covariance matrix in predicting state space parameters is

$$\hat{\mathbf{P}}_{(-)}^{(n-1)} = \mathbf{F}^{(n-1)}\hat{\mathbf{P}}^{(n-3)}{\mathbf{F}^{(n-1)}}^T + \mathbf{Q}^{(n-1)}, \tag{4.2}$$

where $\hat{\mathbf{P}}^{(n-3)}$ is the covariance matrix from previous cycle. The measurements are predicted as

$$\hat{\mathbf{z}}_{(-)}^{(n-1)} = \mathbf{u}^{(n-1)} + \mathbf{h}\left(\hat{\mathbf{x}}_{(-)}^{(n-1)}\right) + \mathbf{v}^{(n-1)}, \tag{4.3}$$

where $\mathbf{h}(\cdot)$ is the non-linear measurement transition function and $\mathbf{v}^{(.)} \sim \mathcal{N}(0, \mathbf{R}^{(.)})$ is the measurement noise assumed to be drawn from a zero-mean, multivariate normal

distribution. The measurement Jacobian $\mathbf{H}$,

$$\mathbf{H}^{(n-1)} = \left.\frac{\partial \mathbf{h}(\hat{\mathbf{x}})}{\partial \hat{\mathbf{x}}}\right|_{\hat{\mathbf{x}}_{(-)}^{(n-1)}} \tag{4.4}$$

is the *acting* measurement transition function. The error covariance matrix in predicting measurements is deduced as

$$\mathbf{S}^{(n-1)} = \mathbf{H}^{(n-1)}\hat{\mathbf{P}}_{(-)}^{(n-1)}\mathbf{H}^{(n-1)^T} + \mathbf{R}^{(n-1)} \tag{4.5}$$

Using these predictions, we correct for the state space variables by evaluating a *weighted sum* of state predictions and deviation in measurement predictions from observations. To do so, we first determine the weighting factor, Kalman gain as,

$$\mathbf{K}^{(n-1)} = \hat{\mathbf{P}}_{(-)}^{(n-1)}\mathbf{H}^{(n-1)^T}\mathbf{S}^{(n-1)^{-1}} \tag{4.6}$$

using which now we can make the following corrections

$$\hat{\mathbf{x}}^{(n-1)} = \hat{\mathbf{x}}_{(-)}^{(n-1)} + \mathbf{K}^{(n-1)}(\mathbf{z}^{(n-1)} - \hat{\mathbf{z}}_{(-)}^{(n-1)}) \tag{4.7}$$

$$\hat{\mathbf{P}}^{(n-1)} = (\mathbf{I}_{|\mathbf{x}|} - \mathbf{K}^{(n-1)}\mathbf{H}^{(n-1)})\hat{\mathbf{P}}_{(-)}^{(n-1)} \tag{4.8}$$

where $|\mathbf{x}|$ is the number of state space parameters. To maintain a resolution of an estimate per frame, we alternate extrapolation amidst tracking. The estimates $\hat{\mathbf{x}}^{(n-1)}$ frame are extrapolated to obtain those at $(n)^{th}$ frame as,

$$\hat{\mathbf{x}}^{(n)} = \mathbf{F}\left(l_A^{(n-1)}\right)\hat{\mathbf{x}}^{(n-1)} \tag{4.9}$$

This construction proves useful for formulating the following first and second order joint delay-offset tracking algorithms.

4.2.2 Adaptive Q Estimation Algorithm

Kalman filtering algorithms rely on knowledge of noise covariance matrices for state and measurements, $\mathbf{Q}$ and $\mathbf{R}$. However, quite often, this knowledge is elusive

Algorithm 1 Extended Kalman Filter Algorithm

while flight duration **do**

$$\hat{\mathbf{x}}_{(-)}^{(n-1)} = \mathbf{F}(L_A^{(n-1)})\,\hat{\mathbf{x}}^{(n-3)}$$

$$\hat{\mathbf{P}}_{(-)}^{(n-1)} = \mathbf{F}^{(n-1)}\hat{\mathbf{P}}^{(n-3)}\mathbf{F}^{(n-1)^T} + \mathbf{Q}^{(n-1)}$$

$$\hat{\mathbf{z}}_{(-)}^{(n-1)} = \mathbf{u}^{(n-1)} + \mathbf{h}(\hat{\mathbf{x}}_{(-)}^{(n-1)})$$

$$\mathbf{H}^{(n-1)} = \left.\frac{\partial \mathbf{h}(\hat{\mathbf{x}})}{\partial \hat{\mathbf{x}}}\right|_{\hat{\mathbf{x}}_{(-)}^{(n-1)}}$$

$$\mathbf{S}^{(n-1)} = \mathbf{H}^{(n-1)}\hat{\mathbf{P}}_{(-)}^{(n-1)}\mathbf{H}^{(n-1)^T} + \mathbf{R}^{(n-1)}$$

$$\hat{\mathbf{z}}_{(-)}^{(n-1)} = \mathbf{u}^{(n-1)} + \mathbf{h}(\hat{\mathbf{x}}_{(-)}^{(n-1)})$$

$$\mathbf{K}^{(n-1)} = \hat{\mathbf{P}}_{(-)}^{(n-1)}\mathbf{H}^{(n-1)^T}\mathbf{S}^{(n-1)^{-1}}$$

$$\hat{\mathbf{x}}^{(n-1)} = \hat{\mathbf{x}}_{(-)}^{(n-1)} + \mathbf{K}^{(n-1)}(\mathbf{z}^{(n-1)} - \hat{\mathbf{z}}_{(-)}^{(n-1)})$$

$$\hat{\mathbf{P}}^{(n-1)} = (\mathbf{I}_{|\mathbf{x}|} - \mathbf{K}^{(n-1)}\mathbf{H}^{(n-1)})\hat{\mathbf{P}}_{(-)}^{(n-1)}$$

end

and unreliable. Instead we can adaptively estimate these noise covariance matrices at every time instance.

This method is inspired from [70] and iterated over for the current problem. The process and measurement noise covariance matrices $\mathbf{Q}$ and $\mathbf{R}$ are dynamic and at any arbitrary time instance, rely on the flight path and oscillator behavior. Hence, they need to be determined on-line. Having access to the performance of ToA estimators, the measurement noise covariance matrix is estimated as

$$\mathbf{R}^{(n-1)} = \text{diag}\left(\, \sigma_{t_{B,Rx}}^{(n-1)\,2}\,,\; \sigma_{t_{A,Rx}}^{(n)\,2}\,\right). \tag{4.10}$$

where $\sigma_{t_{A,Rx}}$ and $\sigma_{t_{B,Rx}}$ are expected deviations at measured integrated SNR. This can be leveraged to estimate process noise covariance $\mathbf{Q}$.

The adaptive estimation of $\mathbf{Q}$ is an iterative process and involves evaluating residue

$\boldsymbol{\Delta}$, in state variables,

$$\boldsymbol{\Delta}_{\mathbf{x}}^{j,(n-1)} = \hat{\mathbf{x}}^{j-1,(n-1)} - \hat{\mathbf{x}}_{(-)}^{(n-1)} \tag{4.11}$$

$$= \mathbf{K}^{j-1,(n-1)} \left(\hat{\mathbf{z}}^{(n-1)} - \hat{\mathbf{z}}_{(-)}^{(n-1)} \right). \tag{4.12}$$

The residue is an indicative of degree of agreement between measurements and models, as is evident from equation (4.12). One source of model mismatch we address in this paper, is noise covariance matrices not being a representative of accrued measurements. In order to correct for this mismatch, we evaluate

$$\boldsymbol{\Delta}_{\mathbf{Q}}^{j,(n-1)} = \hat{\mathbf{P}}^{j,(n-1)} - \mathbf{F}^{(n-1)} \hat{\mathbf{P}}^{(n-3)} \mathbf{F}^{(n-1)^T} \tag{4.13}$$

and compute an intermediary estimate for $\mathbf{Q}$ by compounding the residue $\boldsymbol{\Delta}_{\mathbf{x}}^{(\cdot),(m)}$

Table 4.1: Extended Kalman Filter Notation

$\hat{\mathbf{x}}_{(-)}$, $\hat{\mathbf{x}}$	Predicted and Estimated State Parameters
$\lvert\mathbf{x}\rvert$	Cardinality of state space
$\mathbf{F}$	State Transition Matrix
$\hat{\mathbf{z}}_{(-)}$, $\hat{\mathbf{z}}$	Predicted and Observed Measurements
$\mathbf{u}$	Control Parameters
$\mathbf{h}$, $\mathbf{H}$	Measurement Transition and Jacobian
$\mathbf{w}$, $\mathbf{v}$	State and Measurement Noise
$\mathbf{Q}$, $\mathbf{R}$	State and Measurement Noise Covariance Matrix
$\hat{\mathbf{P}}_{(-)}$, $\hat{\mathbf{P}}$	Predicted and Estimated State Covariance Matrix
$\mathbf{S}$	Measurement Covariance Matrix
$\mathbf{K}$	Kalman Gain

over N previous cycles

$$\mathbf{Q}_{*}^{j,(n-1)} = \mathbf{\Delta}_{\mathbf{Q}}^{j,(n-1)} + \left(\frac{1}{N} \sum_{m=(n-N-1)}^{(n-1)} \mathbf{\Delta}_{\mathbf{x}}^{(\cdot),(m)} \mathbf{\Delta}_{\mathbf{x}}^{(\cdot),(m)^T} \right) \tag{4.14}$$

It is evident from this formulation that the estimation process is heavily influenced by the measurements. CHP2 system in low SNR regimes suffers from measurement outliers. It is therefore, essential to not over-fit the estimation process to the current measurements and can be avoided by curbing how much the noise covariance estimates fluctuate in time. The following weighted sum,

$$\hat{\mathbf{Q}}^{j,(n-1)} = \hat{\mathbf{Q}}^{(n-3)} + \frac{(\mathbf{Q}_{*}^{j,(n-1)} - \hat{\mathbf{Q}}^{(n-3)})}{L_{\mathbf{Q}}^{j}} \tag{4.15}$$

allows for moderating the impact of residuals over the fluctuation of $\mathbf{Q}$. $L_{\mathbf{Q}}^{j}$ a weighting factor that can be assumed constant over all iterations or can be chosen to diminish over multiple iterations.

4.3 Tracking Methods

4.3.1 First Order Markov Model

We leverage the previous formulations to realize ToF tracking while simultaneously synchronizing clocks on two the participating nodes. In this section, we assume that relative propagation delay τ and time offset T between two nodes A and B follow a first order Markov model, hence the title. We model the progression of state space parameters $\mathbf{x}$, in time via the state transition matrix $\mathbf{F}$ as

where the state space variables and transition matrix at any arbitraty frame are

$$\mathbf{x} = \begin{bmatrix} \tau \\ \dot{\tau} \\ T \\ \dot{T} \end{bmatrix}, \; \mathbf{F}\,(l) = \begin{bmatrix} 1 & l & 0 & 0 \\ 0 & 1 & 0 & 0 \\ 0 & 0 & 1 & l \\ 0 & 0 & 0 & 1 \end{bmatrix}. \tag{4.16}$$

and the process noise covariance matrix is modeled as

$$\mathbf{Q}\,(l) = \mathrm{diag}\,(\,\mathbf{Q}_{\tau}(l),\; \mathbf{Q}_{T}(l)\,) \tag{4.17}$$

where $\mathbf{Q}_{\tau}$ and $\mathbf{Q}_{T}$ are covariances in delay and offset transition processes implicating that the two are uncorrelated. The delay covariance $\mathbf{Q}_{\tau} = \mathrm{cov}[\,\tau, \dot{\tau}\,]$ under Gaussian velocity perturbation model [63] is,

$$\mathbf{Q}_{\tau}\,(l) = \begin{bmatrix} \frac{1}{2}\,\sigma^2_{\dot{\tau}}\,l^{\,2} & \sigma^2_{\dot{\tau}}\,l \\ \sigma^2_{\dot{\tau}}\,l & \sigma^2_{\dot{\tau}} \end{bmatrix} \tag{4.18}$$

where $\sigma^2_{\dot{\tau}}$ is variance in relative velocity and relies on perturbations induced by environmental attributes like wind currents. The offset covariance $\mathbf{Q}_{T} = \mathrm{cov}[\,T, \dot{T}\,]$ is a result of two state clock error model [64]

$$\mathbf{Q}_{T}\,(L_A) = \begin{bmatrix} \sigma^2_{T}\,l + \frac{1}{3}\,\sigma^2_{\dot{T}}\,l^{\,3} & \frac{1}{2}\,\sigma^2_{\dot{T}}\,l^{\,2} \\ \frac{1}{2}\,\sigma^2_{\dot{T}}\,l^{\,2} & \sigma^2_{\dot{T}}\,l \end{bmatrix} \tag{4.19}$$

where σ^2_{T} and $\sigma^2_{\dot{T}}$ are variances in estimating relative clock and frequency offset between the two radios.

The measurement transition follows equation (4.3), with measurements and controls being

$$\mathbf{z}^{(n-1)} = \begin{bmatrix} t^{(n-1)}_{B,Rx} \\ t^{(n)}_{A,Rx} \end{bmatrix}, \quad \mathbf{u}^{(n-1)} = \begin{bmatrix} t^{(n-1)}_{A,Tx} \\ t^{(n)}_{B,Tx} \end{bmatrix} \tag{4.20}$$

and the transition function is

$$\mathbf{h}\left(\hat{\mathbf{x}}_{(-)}^{(n-1)}\right) = \begin{bmatrix} \tau^{(n-1)} - T^{(n-1)} \\ \tau^{(n-1)} + \dot{\tau}^{(n-1)}\, l_A^{(n-1)} + \\ T^{(n-1)} + \dot{T}^{(n-1)}\, l_A^{(n-1)} \end{bmatrix}. \tag{4.21}$$

where the first order frame length estimate [20] turns out to be

$$l_A^{1,(n-1)} = \frac{t_{B,Tx}^{(n)} - t_{A,Tx}^{(n-1)} + T^{(n-1)}}{1 - \dot{T}^{(n-1)}}. \tag{4.22}$$

and measurement covariance matrix can be computed using

$$\mathbf{R} = \text{diag}\left(\sigma_{t_{A,Rx}}^2 \,,\, \sigma_{t_{B,Rx}}^2 \right) \tag{4.23}$$

where the variances $\sigma_{t_{A,Rx}}^2$ and $\sigma_{t_{B,Rx}}^2$ rely on performance of the phase-accurate time-of-arrival estimator [18] at any given operational SNR. We derive the measurement Jacobian as

$$\mathbf{H}^{(n-1)} = \left.\frac{\partial \mathbf{h}(\hat{\mathbf{x}})}{\partial \hat{\mathbf{x}}}\right|_{\hat{\mathbf{x}}_{(-)}^{(n-1)}} \tag{4.24}$$

$$= \left[\frac{\partial \mathbf{h}(\hat{\mathbf{x}})}{\partial \tau} \quad \frac{\partial \mathbf{h}(\hat{\mathbf{x}})}{\partial \dot{\tau}} \quad \frac{\partial \mathbf{h}(\hat{\mathbf{x}})}{\partial T} \quad \frac{\partial \mathbf{h}(\hat{\mathbf{x}})}{\partial \dot{T}} \right] \Bigg|_{\hat{\mathbf{x}}_{(-)}^{(n-1)}} \tag{4.25}$$

where

$$\left.\frac{\partial \mathbf{h}(\hat{\mathbf{x}})}{\partial \tau}\right|_{\hat{\mathbf{x}}_{(-)}^{(n-1)}} = \begin{bmatrix} 1 \\ 1 \end{bmatrix} \tag{4.26}$$

$$\left.\frac{\partial \mathbf{h}(\hat{\mathbf{x}})}{\partial \dot{\tau}}\right|_{\hat{\mathbf{x}}_{(-)}^{(n-1)}} = \begin{bmatrix} 0 \\ \frac{t_{B,Tx}^{(n)} - t_{A,Tx}^{(n-1)} + T^{(n-1)}}{1 - T^{(n-1)}} \end{bmatrix} \tag{4.27}$$

$$\left.\frac{\partial \mathbf{h}(\hat{\mathbf{x}})}{\partial T}\right|_{\hat{\mathbf{x}}_{(-)}^{(n-1)}} = \begin{bmatrix} -1 \\ \frac{1 + \dot{\tau}^{(n-1)}}{1 - T^{(n-1)}} \end{bmatrix} \tag{4.28}$$

$$\left.\frac{\partial \mathbf{h}(\hat{\mathbf{x}})}{\partial \dot{T}}\right|_{\hat{\mathbf{x}}_{(-)}^{(n-1)}} = \begin{bmatrix} 0 \\ \frac{(1 + \dot{\tau}^{(n-1)})(t_{B,Tx}^{(n)} - t_{A,Tx}^{(n-1)} + T^{(n-1)})}{(1 - T^{(n-1)})^2} \end{bmatrix} \tag{4.29}$$

4.3.2 Second Order Markov Model

Here, we relax the assumption laid out in the previous section and extend our models to include relative radial acceleration $\ddot{\tau}$ and assume realistic clocks that exhibit frequency drift $\ddot{T}$, which are the second order derivatives, hence the title. The transition matrix, under the second order model, has the structure $\mathbf{F}(L_A) = \text{diag}\,(\,\mathbf{f}(L_A)\,,\,\mathbf{f}(L_A)\,)$, where the state space variables and trasition matrix are

$$\mathbf{x} = \begin{bmatrix} \tau \\ \dot{\tau} \\ \ddot{\tau} \\ T \\ \dot{T} \\ \ddot{T} \end{bmatrix}\,,\ \mathbf{f}(l) = \begin{bmatrix} 1 & l & \frac{1}{2}l^2 \\ 0 & 1 & l \\ 0 & 0 & 1 \end{bmatrix} \tag{4.30}$$

Under Gaussian acceleration perturbation model, the delay covariance $\mathbf{Q}_\tau = \text{cov}[\,\tau, \dot{\tau}, \ddot{\tau}\,]$ reduces to,

$$\mathbf{Q}_\tau\,(l) = \begin{bmatrix} \frac{1}{4}\,\sigma^2_{\ddot{\tau}}\,l^4 & \frac{1}{2}\,\sigma^2_{\ddot{\tau}}\,l^3 & \frac{1}{2}\,\sigma^2_{\ddot{\tau}}\,l^2 \\ \frac{1}{2}\,\sigma^2_{\ddot{\tau}}\,l^3 & \frac{1}{2}\,\sigma^2_{\ddot{\tau}}\,l^2 & \sigma^2_{\ddot{\tau}}\,l \\ \frac{1}{2}\,\sigma^2_{\ddot{\tau}}\,l^2 & \sigma^2_{\ddot{\tau}}\,l & \sigma^2_{\ddot{\tau}} \end{bmatrix} \tag{4.31}$$

where $\sigma^2_{\ddot{\tau}}$ is variance in relative acceleration and it relies on perturbations induced by environment. The offset covariance $\mathbf{Q}_T = \text{cov}[\,T, \dot{T}, \ddot{T}\,]$ is a reflection of errors in clocks dictated by their Allan variance characteristics. Under the current formulation, the offset covariance [60]

$$\mathbf{Q}_T\,(l) = \sigma^2_T\,q_1\,(l) + \sigma^2_{\dot{T}}\,q_2\,(l) + \sigma^2_{\ddot{T}}\,q_3\,(l) \tag{4.32}$$

with

$$q_1(l) = \begin{bmatrix} l & 0 & 0 \\ 0 & 0 & 0 \\ 0 & 0 & 0 \end{bmatrix} \quad q_2(L_A) = \begin{bmatrix} \frac{1}{3}l^3 & \frac{1}{2}l^2 & 0 \\ \frac{1}{2}l^2 & l & 0 \\ 0 & 0 & 0 \end{bmatrix} \quad q_3(L_A) = \begin{bmatrix} \frac{1}{20}l^5 & \frac{1}{8}l^4 & \frac{1}{6}l^3 \\ \frac{1}{8}l^4 & \frac{1}{3}l^3 & \frac{1}{2}l^2 \\ \frac{1}{6}l^3 & \frac{1}{2}l^2 & l \end{bmatrix} \tag{4.33}$$

The clock error model is fit to the Allan variance of the oscillators in use to extract the model parameters σ_T^2 , $\sigma_{\dot{T}}^2$ and $\sigma_{\ddot{T}}^2$, but this discussion is out of scope for this report and shall be addressed in accompanying publications.

The measurement transition model is

$$\hat{\mathbf{z}}_{(-)}^{(n-1)} = \mathbf{u}^{(n-1)} + \mathbf{h}\left(\hat{\mathbf{x}}_{(-)}^{(n-1)}\right) + \mathbf{v}^{(n-1)}, \tag{4.34}$$

where $\hat{z}^{(k)}$ are the measurements, $u^{(k)}$ is the control vector at $(k)^{th}$ frame, subscript $_{(-)}$ indicates prediction,

$$\hat{\mathbf{z}}_{(-)}^{(n-1)} = \begin{bmatrix} t_{B,Rx}^{(n-1)} \\ t_{A,Rx}^{(n)} \end{bmatrix}, \quad \mathbf{u}^{(n-1)} = \begin{bmatrix} t_{A,Tx}^{(n-1)} \\ t_{B,Tx}^{(n)} \end{bmatrix} \tag{4.35}$$

where the transition function $\mathbf{h}(\cdot)$ now becomes

$$\mathbf{h}\left(\hat{\mathbf{x}}_{(-)}^{(n-1)}\right) = \begin{bmatrix} \tau^{(n-1)} - T^{(n-1)} \\ \tau^{(n-1)} + \dot{\tau}^{(n-1)}\, l_A^{(n-1)} + \ddot{\tau}^{(n-1)}\, {l_A^{(n-1)}}^2 + \\ T^{(n-1)} + \dot{T}^{(n-1)}\, l_A^{(n-1)} + \ddot{T}^{(n-1)}\, {l_A^{(n-1)}}^2 \end{bmatrix} \tag{4.36}$$

where second order estimate of frame length [20] is derived as

$$l_A^{2,(n-1)} = \frac{\beta^{(n-1)} - \sqrt{\hat{\beta}^{(n-1)^2} - 2\,\alpha^{(n-1)}\gamma^{(n-1)}}}{\alpha^{(n-1)}} \tag{4.37}$$

with

$$\nu^{(n-1)} = \hat{\beta}^{(n-1)^2} - 2\,\alpha^{(n-1)}\gamma^{(n-1)} \tag{4.38}$$

$$\alpha^{(n-1)} = \ddot{T}^{(n-1)} \quad , \quad \beta^{(n-1)} = 1 - T^{(n-1)} \tag{4.39}$$

$$\gamma^{(n-1)} = T^{(n-1)} + t_{B,Tx}^{(n)} - t_{A,Tx}^{(n-1)} \tag{4.40}$$

$\mathbf{v}^{(\cdot)} \sim \mathcal{N}(0, \mathbf{R}^{(\cdot)})$ is the measurement noise with covariance $\mathbf{R}^{(\cdot)} = \text{diag}\left(t_{A,Rx}^{(\cdot)}, t_{B,Rx}^{(\cdot)} \right)$ indicated in (4.23).

The measurement Jacobian $\mathbf{H}^{(n-1)}$ is derived as,

$$\mathbf{H}^{(n-1)} = \left.\frac{\partial \mathbf{h}(\hat{\mathbf{x}})}{\partial \hat{\mathbf{x}}}\right|_{\hat{\mathbf{x}}_{(-)}^{(n-1)}} = \left.\left[\frac{\partial \mathbf{h}(\hat{\mathbf{x}})}{\partial \tau} \quad \frac{\partial \mathbf{h}(\hat{\mathbf{x}})}{\partial \dot{\tau}} \quad \frac{\partial \mathbf{h}(\hat{\mathbf{x}})}{\partial \ddot{\tau}} \quad \frac{\partial \mathbf{h}(\hat{\mathbf{x}})}{\partial T} \quad \frac{\partial \mathbf{h}(\hat{\mathbf{x}})}{\partial T} \quad \frac{\partial \mathbf{h}(\hat{\mathbf{x}})}{\partial T}\right]\right|_{\hat{\mathbf{x}}_{(-)}^{(n-1)}} \tag{4.41}$$

where

$$\left.\frac{\partial \mathbf{h}(\hat{\mathbf{x}})}{\partial \tau}\right|_{\hat{\mathbf{x}}_{(-)}^{(n-1)}} = \begin{bmatrix} 1 \\ 1 \end{bmatrix} \tag{4.42}$$

$$\left.\frac{\partial \mathbf{h}(\hat{\mathbf{x}})}{\partial \dot{\tau}}\right|_{\hat{\mathbf{x}}_{(-)}^{(n-1)}} = \begin{bmatrix} 0 \\ l_A^{(n-1)} \end{bmatrix} \tag{4.43}$$

$$\left.\frac{\partial \mathbf{h}(\hat{\mathbf{x}})}{\partial \ddot{\tau}}\right|_{\hat{\mathbf{x}}_{(-)}^{(n-1)}} = \begin{bmatrix} 0 \\ \frac{1}{2}\, l_A^{(n-1)^2} \end{bmatrix} \tag{4.44}$$

$$\left.\frac{\partial \mathbf{h}(\hat{\mathbf{x}})}{\partial T}\right|_{\hat{\mathbf{x}}_{(-)}^{(n-1)}} = \begin{bmatrix} -1 \\ 1 + \left(\dot{\tau}^{(n-1)} + T^{(n-1)}\right) \left.\frac{\partial l_A(\hat{\mathbf{x}})}{\partial T}\right|_{\hat{\mathbf{x}}_{(-)}^{(n-1)}} \\ + \left(\ddot{\tau}^{(n-1)} + \ddot{T}^{(n-1)}\right) l_A^{(n-1)} \left.\frac{\partial l_A(\hat{\mathbf{x}})}{\partial T}\right|_{\hat{\mathbf{x}}_{(-)}^{(n-1)}} \end{bmatrix} \tag{4.45}$$

$$\left.\frac{\partial \mathbf{h}(\hat{\mathbf{x}})}{\partial T}\right|_{\hat{\mathbf{x}}_{(-)}^{(n-1)}} = \begin{bmatrix} 0 \\ l_A^{(n-1)} + \left(\dot{\tau}^{(n-1)} + T^{(n-1)}\right) \left.\frac{\partial l_A(\hat{\mathbf{x}})}{\partial T}\right|_{\hat{\mathbf{x}}_{(-)}^{(n-1)}} \\ + \left(\ddot{\tau}^{(n-1)} + \ddot{T}^{(n-1)}\right) l_A^{(n-1)} \left.\frac{\partial l_A(\hat{\mathbf{x}})}{\partial T}\right|_{\hat{\mathbf{x}}_{(-)}^{(n-1)}} \end{bmatrix} \tag{4.46}$$

$$\left.\frac{\partial \mathbf{h}(\hat{\mathbf{x}})}{\partial T}\right|_{\hat{\mathbf{x}}_{(-)}^{(n-1)}} = \begin{bmatrix} 0 \\ \frac{1}{2} l_A^{(n-1)^2} + \left(\dot{\tau}^{(n-1)} + T^{(n-1)}\right) \left.\frac{\partial l_A(\hat{\mathbf{x}})}{\partial T}\right|_{\hat{\mathbf{x}}_{(-)}^{(n-1)}} \\ + \left(\ddot{\tau}^{(n-1)} + \ddot{T}^{(n-1)}\right) l_A^{(n-1)} \left.\frac{\partial l_A(\hat{\mathbf{x}})}{\partial T}\right|_{\hat{\mathbf{x}}_{(-)}^{(n-1)}} \end{bmatrix} \tag{4.47}$$

with

$$\left.\frac{\partial l_A(\hat{\mathbf{x}})}{\partial T}\right|_{\hat{\mathbf{x}}_{(-)}^{(n-1)}} = \frac{1}{\nu^{(n-1)}} \tag{4.48}$$

$$\left.\frac{\partial l_A(\hat{\mathbf{x}})}{\partial T}\right|_{\hat{\mathbf{x}}_{(-)}^{(n-1)}} = \frac{-1}{\ddot{T}^{(n-1)}}\left(\frac{T^{(n-1)}-1}{\nu^{(n-1)}}+1\right) \tag{4.49}$$

$$\left.\frac{\partial l_A(\hat{\mathbf{x}})}{\partial T}\right|_{\hat{\mathbf{x}}_{(-)}^{(n-1)}} = \frac{T^{(n-1)}-t_{A,Tx}^{(n-1)}+t_{B,Tx}^{(n-1)}}{\ddot{T}^{(n-1)}\nu^{(n-1)}}+\frac{\nu^{(n-1)}+T^{(n-1)}-1}{\ddot{T}^{(n-1)^2}} \tag{4.50}$$

4.4 Simulations

We study through simulations, performance of the first and second order joint delay-offset EKF tracking methods. We compare performance of tracking methods to optimal one-shot estimators portrayed in previous chapter. We simulated a stationary, ground user A and a mobile, airborne user B following an arbitrary flight path (Figure 4.1).

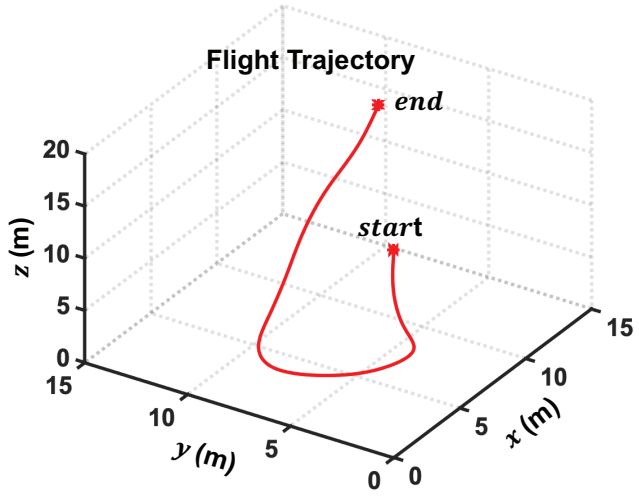

Figure 4.1: Simulated Flight Trajectory Of User B For 60 Seconds. User A Is Stationary, Situated At The Origin.

The two nodes co-operatively exchange timing information every frame which are $\hat{l}_A = 50$ ms apart. The transmit timestamps $t_{A,Tx}$ and $t_{B,Tx}$ are assumed to

be known with certainty and the receive timestamps $\hat{t}_{A,Rx}$ and $\hat{t}_{B,Rx}$ are a result of carrier-phase-accurate time of arrival (ToA) estimation and are known to a precision σ_{ToA}. We are interested in the regime where SNR of the received signal in this two-way communication between participating nodes exceeds 45 dB, resulting in ToA estimates that are precise at least up to 3cm $\sim 1^{-10}$ s [9]. We employ first and second order optimal estimators delineated in [20] and Extended Kalman Filter tracking methods mentioned in Sections IV and V to estimate propagation delay τ and time offset T for the simulated scenarios. We compare their performance via standard deviation in delay $\sigma_\tau = \hat{\tau} - \tau_{true}$ and offset $\sigma_T = \hat{T} - T_{true}$.

4.5 Summary

Limited spectral access motivates radio technologies that are capable of performing multiple tasks simultaneously and efficiently cooperating with existing systems. We develop a joint positioning- communications system for a vehicular ad hoc network that simultaneously synchronizes distributed users, performs carrier-phase-accurate localization, and enables network communications. In this paper, we focus on two-way ranging methods for jointly estimating propagation delay and clock offset between the nodes in the network. We propose Extended Kalman Filter (EKF) for first and second order methods to achieve distributed phase coherence while jointly estimating time-of-flight (ToF) between them. We demonstrate their workings for simulated flight paths, study their performance and identify their region of applicability. We extended this formulation for higher order models on state space parameters and to joint delay-offset estimation in multiple antenna systems.

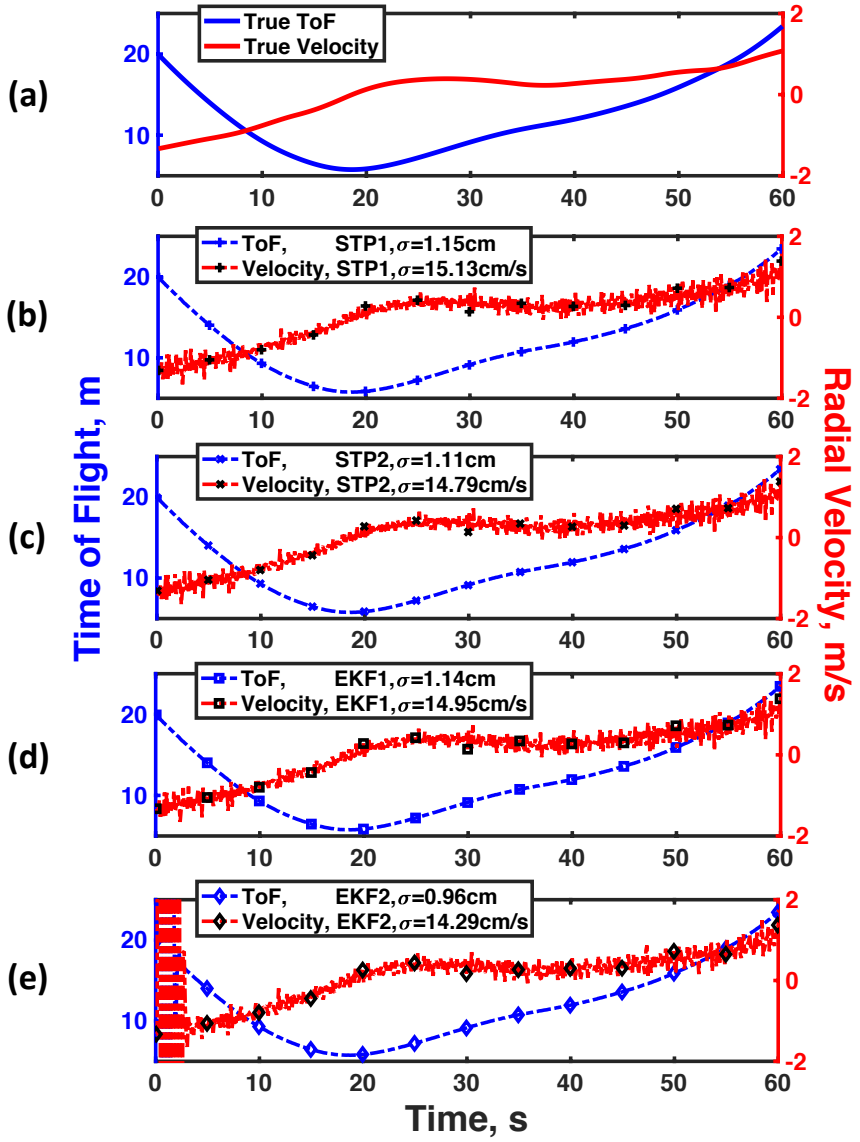

Figure 4.2: True And Estimated Relative ToF And Velocity Between The Two Users. The EKF Estimates, Indicated Here At Every Measurement Instance, The ToF Estimates Are Precise Upto 1.2 Cm.

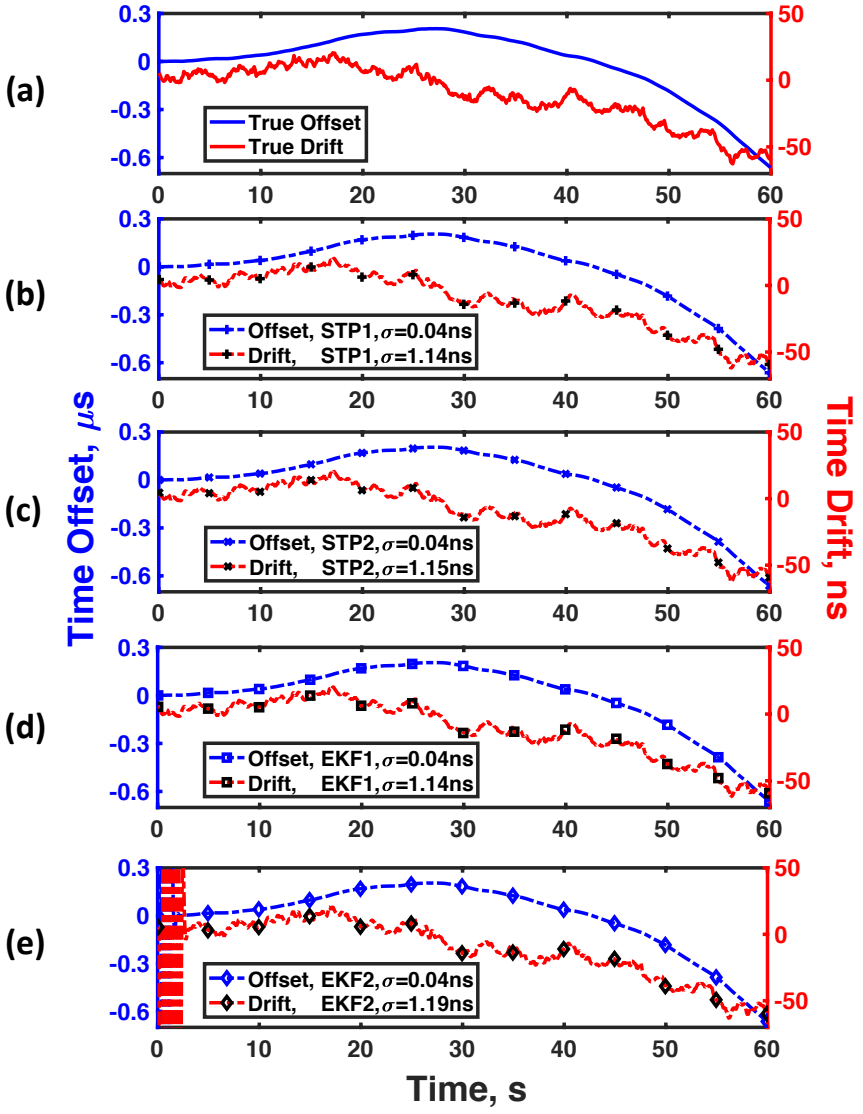

Figure 4.3: True And Estimated Relative Clock Offset And Drift Of The Aerial Node With Respect To The Ground Node. The EKF Estimates, Indicated Here At Every Measurement Instance, The Clcok Offset Estimates Are Precise Upto A 0.04ns.

Chapter 5

JOINT POSITION AND ORIENTATION TRACKING

Future radio systems must rely on co-existence and co-operation techniques to adapt to limited spectral resources and increasing demand. Motivated by the promise of RF Convergence co-design techniques, we designed and implemented the Communications and High-Precision Positioning (CHP2) system for flying ad hoc networks (FANETs). CHP2 simultaneously synchronizes distributed users, performs carrier-phase-accurate localization and enables network communications using limited bandwidth. We previously demonstrated rapid (<100 ms) and precise (<1 cm) ranging capabilities using limited spectrum bandwidth (10 MHz) in over-the-air experiments using re-configurable base stations and unmanned aerial systems (UASs). In this study, we investigate methods of leveraging these ranging estimates to localize multi-antenna users. We discuss joint position and orientation tracking methodologies for multi-antenna platforms that leverage time-of-flight (ToF) estimates between cross-platform antenna pairs. This formulation is novel and accurately represents a target's movement as an integration of its translation and rotation. We assert that the these capabilities make CHP2 a suitable candidate to provide both communications, navigation, and surveillance (CNS) and alternative positioning, navigation, and timing (APNT) services for safety-critical transport applications on a variety of vehicular platforms.

CHP2 system leverages two-way ranging (TWR) between multi-antenna platforms to simultaneously enable distributed phase coherence, carrier-phase-accurate ranging, and network communications from a single radio platform. Multi-antenna CHP2 users estimate the range between each cross-platform antenna pair, which provides

sufficient spatial diversity to estimate relative position and orientation. Given the extreme precision of these range estimates, even moderately small platforms such as UASs may be precisely localized. In this study, we investigate methods of leveraging these ranging estimates to localize multi-antenna users. We discuss joint position and orientation tracking methodologies for multi-antenna platforms that leverage time-of-flight (ToF) estimates between cross-platform antenna pairs. This formulation is novel and accurately represents a target's movement as an integration of its translation and rotation.

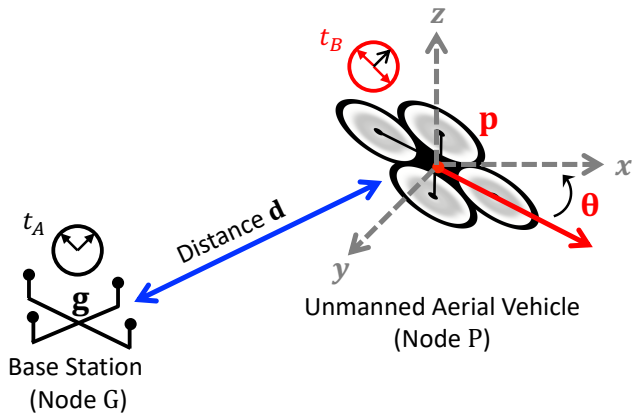

Figure 5.1: CHP2 Users Estimate The Distance Between Each Cross-Platform Pair Of Antennas Using A Two-Way Ranging Algorithm And Cyclic Timing Exchange. For Multi-Antenna Users, This Spatial Diversity May Be Leveraged To Estimate The Relative Position And Orientation Of Other CHP2 Users.

5.1 Prior Work and Contributions

In this paper we leverage these ToF estimates to jointly localize and determine orientation of the targets when communicating over a multi-antenna waveforms. Prior work in this field is identified as follows:

Position Estimation Time-of-arrival (ToA) based localization of participating

nodes has been studied over the past few decades [13]. In conjunction, several estimators were proposed and their performance was studied in [14], CRLB were derived on position estimation [15] and GDOP of different localization techniques was investigated in [16]; we focus on geometric interpretations of theoretical results.

Orientation Estimation Traditionally on-board IMUs are used to determine attitude of a aerial nodes and filtering techniques are implemented to track these rotations in time [17]. Instead in this system, multi antenna radios on each node enable orientation estimation of surrounding nodes in the network purely based on the ToA estimates.

The novel contribution of the paper to this field are as follows

- Propose a novel Extended Kalman Filter (EKF) formulation to simultaneously track position and orientation on of a target in a multi-antenna joint positioning-communications network.
- Demonstrate centimeter level positioning capabilities and orientation precise up to a few degrees.

5.2 Setup

Nodes in the joint positioning-communications system communicate with nearby nodes over multiple antennae radio platforms and a phase accurate variant of network timing protocol (NTP) is used to synchronize their clocks [9]. Any two nodes in this network consecutively transmit and receive communication signal and estimate ToF between each antennae pair by computing time difference of signal transmission and reception time stamps which are then translated into relative position and orientation of the other nodes.

To demonstrate workings of the system, we put forth a network of two identical nodes $\mathbf{g}$ and $\mathbf{p}$, see Figure 5.1, communicating via an N antennae radios, indicated by

subscripts. For the sake of simplicity, the ground node $\mathbf{g}$ is assumed to be stationary while node $\mathbf{p}$ is moving. Both the nodes estimate time-of-flight (ToF) between each cross-platform antenna pair by observing time stamps of transmission and reception events. In this paper, we are interested in uncovering bounds on how well these ToF estimates can be translated into relative position and attitude of $\mathbf{p}$ w.r.t $\mathbf{g}$ and exploring estimators for a two dimensional scenario.

5.3 Joint Position and Orientation Tracking

CHP2 users simultaneously execute communications and positioning tasks. Users alternate transmitting and receiving a multi-function waveform that contains several navigation reference sequences and a communications payload. Each navigation sequence is transmitted from a different antenna and are used to estimate the ToA at each receive antenna. The communications payload contains timing information that drives a ToF estimation algorithm at the receiver. This cyclic exchange allows CHP2 users to digitally synchronize their clock sources and precisely estimate relative position and orientation.

5.3.1 Problem Formulation

For the current setup we consider two identical nodes $\mathbf{g}$ and $\mathbf{p}$ communicating over an N antennae radios indicated by subscripts, see Figure 5.1. CHP2 is capable of joint distributed coherence and precise ToF estimation [20] which we leverage to localize targets. The relative ToF estimates between cross-platform radios are assumed to be a result of line-of-sight (LoS) channel between the transmit-receive pairs. We derive distances between ground node antenna $\mathbf{g}_i$ and aerial node antenna $\mathbf{p}_j$

$$d_{i,j} = \sqrt{\sum_{x,y,z} \left[\mathbf{g}_i - \mathbf{p}_j\right]^2} \tag{5.1}$$

as $d_{i,j} = c\,\tau_{i,j}$ where c is the speed of light in vacuum and τ indicate ToF estimates. Antennae $\mathbf{p}_j$ are related to the location of the target $\mathbf{p} = [p_x, p_y, p_z]$, see Figure 5.2, under the assumption that the relative location $\boldsymbol{\pi}_j$ of the antennae are known, as

$$\mathbf{p}_j = \mathbf{p} + \mathbf{R}(\boldsymbol{\theta})\,\boldsymbol{\pi}_j \tag{5.2}$$

where $\boldsymbol{\theta} = [\theta_x, \theta_y, \theta_z]$ is the orientation of the target in three dimensional space and $\mathbf{R}$ is the right-handed rotation matrix,

$$\mathbf{R}\,(\boldsymbol{\theta}) = \mathbf{R}_x(\theta_x)\mathbf{R}_y(\theta_y)\mathbf{R}_z(\theta_z) \tag{5.3}$$

defined as a product of rotations in each of the directions.

5.3.2 Tracking Preliminaries

We intend to jointly track position, orientation of the target while we only have access to distances between transmit-receive antennae pairs and we leverage Kalman Filtering[56] ideology to do so. We model the time progression of state space parameters using Markov models, represented here as

$$\hat{\mathbf{x}}^{(n)}_{(-)} = \mathbf{F}\left(L_A^{(n)}\right)\,\hat{\mathbf{x}}^{(n-1)} + \mathbf{w}^{(n)} \tag{5.4}$$

where $\mathbf{w}^{(\cdot)} \sim \mathcal{N}(0, \mathbf{Q}^{(\cdot)})$ is the process noise, assumed to be drawn from a zero mean multivariate normal distribution and $L_A^{(n)}$ is the time elapsed from previous measurement instance. The state space variables are

$$\mathbf{x} = \begin{bmatrix} \mathbf{p} & \mathbf{v} & \mathbf{a} & \boldsymbol{\theta} & \boldsymbol{\omega} \end{bmatrix}^T \tag{5.5}$$

where each is a three dimensional vector to constitute the motion in a 3D Cartesian space, for example $\mathbf{p} = [p_x, p_y, p_z]$. The state transition matrix $\mathbf{F}\,(L_A)$ is derived from

the following

$$\mathbf{p}^{(n)} = \mathbf{p}^{(n-1)} + L_A^{(n)}\,\mathbf{v}^{(n-1)} + \frac{1}{2}\,{L_A^{(n)}}^2\mathbf{a}^{(n-1)} \tag{5.6}$$

$$\mathbf{v}^{(n)} = \mathbf{v}^{(n-1)} + L_A^{(n)}\,\mathbf{a}^{(n-1)} \tag{5.7}$$

$$\mathbf{a}^{(n)} = \mathbf{a}^{(n-1)} \tag{5.8}$$

$$\boldsymbol{\theta}^{(n)} = \boldsymbol{\theta}^{(n-1)} + L_A^{(n)}\,\boldsymbol{\omega}^{(n-1)} \tag{5.9}$$

$$\boldsymbol{\omega}^{(n)} = \boldsymbol{\omega}^{(n-1)} \tag{5.10}$$

The predicted state covariance matrix is

$$\hat{\mathbf{P}}_{(-)}^{(n)} = \mathbf{F}^{(n)}\,\hat{\mathbf{P}}^{(n-1)}\,{\mathbf{F}^{(n)}}^T + \mathbf{Q}^{(n)} \tag{5.11}$$

where $\hat{\mathbf{P}}^{(n-1)}$ is the error covariance matrix from previous cycle and $\mathbf{F}^{(n)}$ is used as a short hand for $\mathbf{F}(L_A^{(n)})$. The measurement transition is modeled as

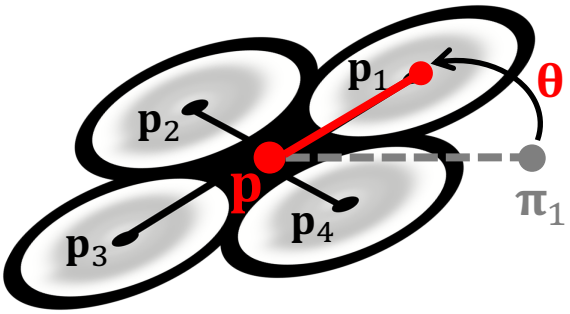

Figure 5.2: Target Antennae Locations $\mathbf{p}_j$ When The Target Location Is $\mathbf{p}$ And Orientation Is $\boldsymbol{\theta}$ Under The Assumption That The Relative Location $\boldsymbol{\pi}_j$ Of The Antennae Are Known.

$$\hat{\mathbf{z}}_{(-)}^{(n)} = \mathbf{h}\left(\hat{\mathbf{x}}_{(-)}^{(n)}\right) + \mathbf{v}^{(n)} \tag{5.12}$$

with $\mathbf{v}^{(\cdot)} \sim \mathcal{N}(0, \mathbf{R}^{(\cdot)})$ is the measurement noise, drawn from a zero mean multivariate normal distribution and $\mathbf{h}(\cdot)$ using equations (5.1) - (5.3), as

$$\mathbf{h}\left(\hat{\mathbf{x}}_{(-)}^{(n)}\right) = \sqrt{\sum_{x,y,z}\left[\mathbf{g}_i^{(n)} - \hat{\mathbf{p}}^{(n)} - \mathbf{R}(\hat{\boldsymbol{\theta}}^{(n)})\,\boldsymbol{\pi}_j\right]^2} \tag{5.13}$$

Since the measurement function is highly non-linear, we rely on Jacobian function to linearize $\mathbf{h}$. The measurement Jacobian $\mathbf{H}$ is derived below.

$$\mathbf{H}^{(n-1)}\big|_{\hat{\mathbf{x}}_{(-)}^{(n)}} = \begin{bmatrix} \frac{\partial}{\partial \mathbf{p}}\hat{d}_{1,1}^{(n)} & \frac{\partial}{\partial \mathbf{v}}\hat{d}_{1,1}^{(n)} & \frac{\partial}{\partial \mathbf{a}}\hat{d}_{1,1}^{(n)} & \frac{\partial}{\partial \boldsymbol{\theta}}\hat{d}_{1,1}^{(n)} & \frac{\partial}{\partial \boldsymbol{\omega}}\hat{d}_{1,1}^{(n)} \\ \vdots & \vdots & \vdots & \vdots & \vdots \\ \frac{\partial}{\partial \mathbf{p}}\hat{d}_{i,j}^{(n)} & \frac{\partial}{\partial \mathbf{v}}\hat{d}_{i,j}^{(n)} & \frac{\partial}{\partial \mathbf{a}}\hat{d}_{i,j}^{(n)} & \frac{\partial}{\partial \boldsymbol{\theta}}\hat{d}_{i,j}^{(n)} & \frac{\partial}{\partial \boldsymbol{\omega}}\hat{d}_{i,j}^{(n)} \\ \vdots & \vdots & \vdots & \vdots & \vdots \\ \frac{\partial}{\partial \mathbf{p}}\hat{d}_{I,J}^{(n)} & \frac{\partial}{\partial \mathbf{v}}\hat{d}_{I,J}^{(n)} & \frac{\partial}{\partial \mathbf{a}}\hat{d}_{I,J}^{(n)} & \frac{\partial}{\partial \boldsymbol{\theta}}\hat{d}_{I,J}^{(n)} & \frac{\partial}{\partial \boldsymbol{\omega}}\hat{d}_{I,J}^{(n)} \end{bmatrix}\Bigg|_{\hat{\mathbf{x}}_{(-)}^{(n)}} \tag{5.14}$$

Here distance is indicated as estimates since the time-of-flight is a result of prior estimation methods. The partial derivative from equation 5.14 are

$$\frac{\partial}{\partial \mathbf{p}}\hat{d}_{i,j}^{(n)}\Big|_{\hat{\mathbf{x}}_{(-)}^{(n)}} = \frac{\hat{\mathbf{p}}^{(n)} - \mathbf{g}_i^{(n)} + \mathbf{R}(\hat{\boldsymbol{\theta}}^{(n)})\Big|_{\hat{\mathbf{x}}_{(-)}^{(n)}} \boldsymbol{\pi}_j}{\hat{d}_{i,j}^{(n)}} \tag{5.15}$$

$$\frac{\partial}{\partial \mathbf{v}}\hat{d}_{i,j}^{(n)}\Big|_{\hat{\mathbf{x}}_{(-)}^{(n)}} = 0 \tag{5.16}$$

$$\frac{\partial}{\partial \mathbf{a}}\hat{d}_{i,j}^{(n)}\Big|_{\hat{\mathbf{x}}_{(-)}^{(n)}} = 0 \tag{5.17}$$

$$\frac{\partial}{\partial \boldsymbol{\theta}}\hat{d}_{i,j}^{(n)}\Big|_{\hat{\mathbf{x}}_{(-)}^{(n)}} = \frac{\left[\hat{\mathbf{p}}_j^{(n)} - \mathbf{g}_i^{(n)}\right]^T \frac{\partial}{\partial \boldsymbol{\theta}}\mathbf{R}(\hat{\boldsymbol{\theta}}^{(n)})\Big|_{\hat{\mathbf{x}}_{(-)}^{(n)}} \boldsymbol{\pi}_j}{\hat{d}_{i,j}^{(n)}} \tag{5.18}$$

$$\frac{\partial}{\partial \boldsymbol{\omega}}\hat{d}_{i,j}^{(n)}\Big|_{\hat{\mathbf{x}}_{(-)}^{(n)}} = 0 \tag{5.19}$$

where the derivative of rotation matrix can be derived as a product of derivative of rotations in each dimension,

$$\frac{\partial}{\partial \boldsymbol{\theta}}\mathbf{R}\left(\boldsymbol{\theta}\right) = \left[\frac{\partial}{\partial \theta_x}\mathbf{R}_x(\theta_x),\ \frac{\partial}{\partial \theta_y}\mathbf{R}_y(\theta_y),\ \frac{\partial}{\partial \theta_z}\mathbf{R}_z(\theta_z)\right]^T \tag{5.20}$$

We further simplify these derivative using the identities

$$\frac{\partial}{\partial\theta_x}\mathbf{R}_x(\theta_x) = \mathbf{S}[1,0,0]\,\mathbf{R}_x(\theta_x) \tag{5.21}$$

$$\frac{\partial}{\partial\theta_y}\mathbf{R}_y(\theta_y) = \mathbf{S}[0,1,0]\,\mathbf{R}_y(\theta_y) \tag{5.22}$$

$$\frac{\partial}{\partial\theta_z}\mathbf{R}_z(\theta_z) = \mathbf{S}[0,0,1]\,\mathbf{R}_z(\theta_z) \tag{5.23}$$

where the matrix $\mathbf{S}$ is

$$\mathbf{S}[a,b,c] = \begin{bmatrix} 0 & -c & b \\ c & 0 & -a \\ -b & a & 0 \end{bmatrix} \tag{5.24}$$

With this formulation, one could jointly track position and orientation of the target $\mathbf{p}$.

5.4 Simulation Results

We demonstrate that the joint position and orientation tracking methodology in the context of CHP2. We simulated a stationary, ground user $\mathbf{g}$ and a mobile, airborne user $\mathbf{p}$ following an arbitrary flight path (Figure 5.3). The two nodes operate over a 4×4 multi-antenna system. The ground node antennae at 2 meters apart centered at origin along the x direction, 1 m in y direction and 2m in z direction. The aerial node antennae relative to the center of its body are one 2 meters apart in both x and y directions. The simulated flight trajectory is highly non-linear with position an orientation of the target changing constantly, hence non-trivial. With this setup we study the performance of the joint tracking algorithm.

We assume that the state and measurement noise covariance matrices are known *a priori*. These may be adaptively estimated in real time but this discussion is beyond the scope of this report. We model these matrices as a function of integrated signal to

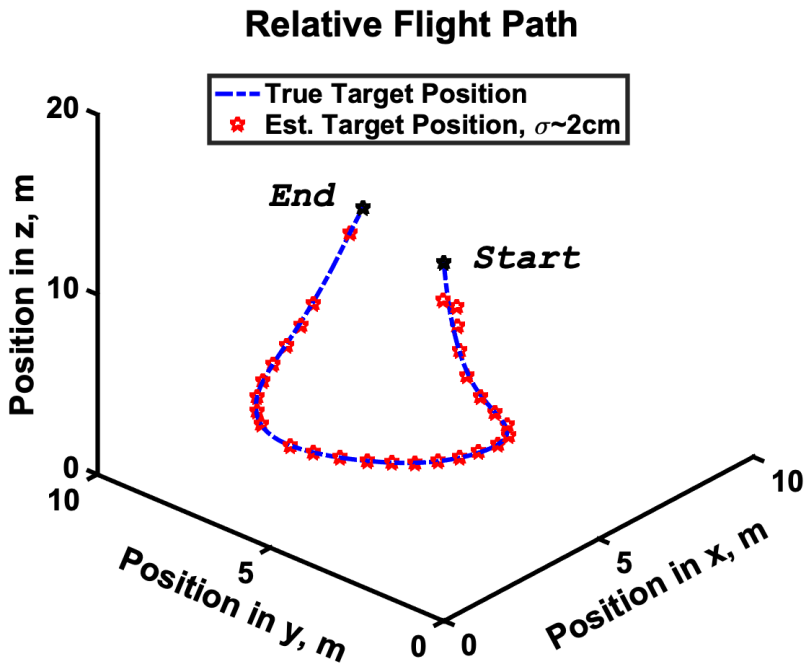

Figure 5.3: Simulated And Estimated Flight Trajectory Of User B For 40 Seconds. User A Is Stationary, Situated At The Origin. The EKF Estimates Are Precise Upto 2 Cm.

noise ratio (SNR) to fit the flight trajectory. CHP2 operates with 30 dB of waveform integration gain and maintains an operational instantaneous SNR of 15 dB, which yields ToA estimates precise to within 0.1 ns (3 cm) [9].

In Figure 5.4, we demonstrate how the antennae are aligned with respect to the location of the target on the aerial node. Figure 5.5 depicts the relative distance between radios $\mathbf{g}_1$ and $\mathbf{p}_j$ for all $j \in (1, 4)$. We now study the performance of the joint position and orientation tracking method using Extended Kalman Filters (EKF). Plots in Figures 5.6 and 5.7 show the relative location and orientation of the aerial node $\mathbf{p}$ w.r.t the ground node $\mathbf{g}$, respectively. The filtering estimates are precise upto 2 cm in positioning and within 2° in estimating orientation in each of the directions of a Cartesian space.

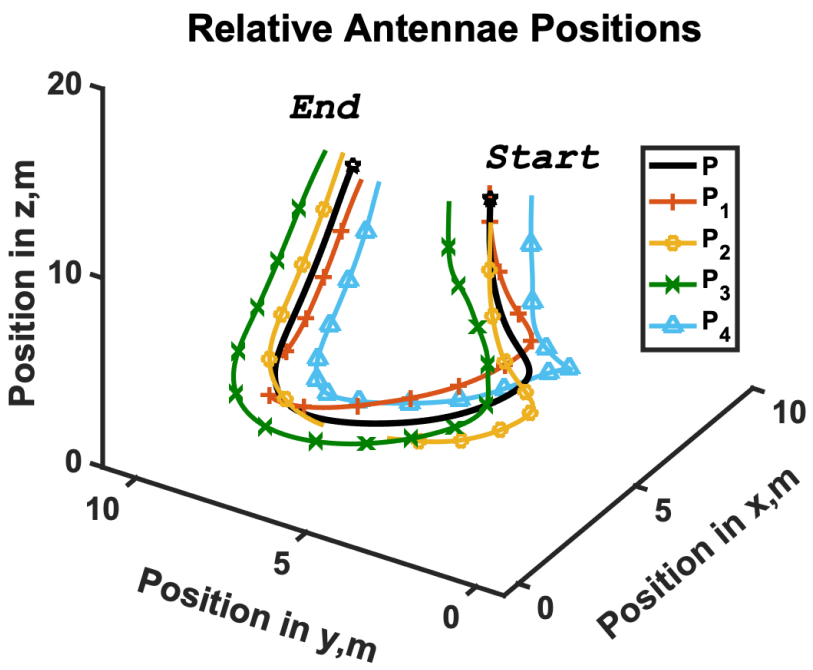

Figure 5.4: Location Of Aerial Node $\mathbf{p}$ And Its Antennae $\mathbf{p}_j$ For The Entirety Of The Flight Trajectory.

5.5 Summary

Limited spectral resources drive future radio systems co-existence and co-operation techniques. This motivated us to build a Communications and High-Precision Positioning (CHP2) to provide communications, navigation, and surveillance (CNS) and alternative positioning, navigation, and timing (APNT) services to flying ad hoc networks (FANETs). Participating multi-antenna nodes in the network engage in two-way ranging (TWR) protocol. In this paper, we formulate a joint position and orientation tracking algorithm in the context of this novel system. We demonstrated centimeter level positioning and degree level orientation results for simulated flight paths.

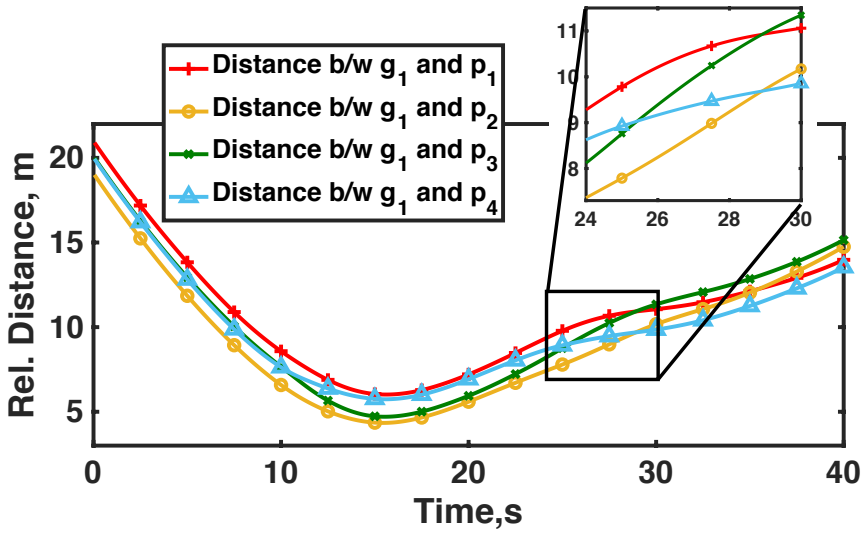

Figure 5.5: Relative Distance Between Radios $\mathbf{g}_1$ and $\mathbf{p}_j$ for all $j \in (1, 4)$.

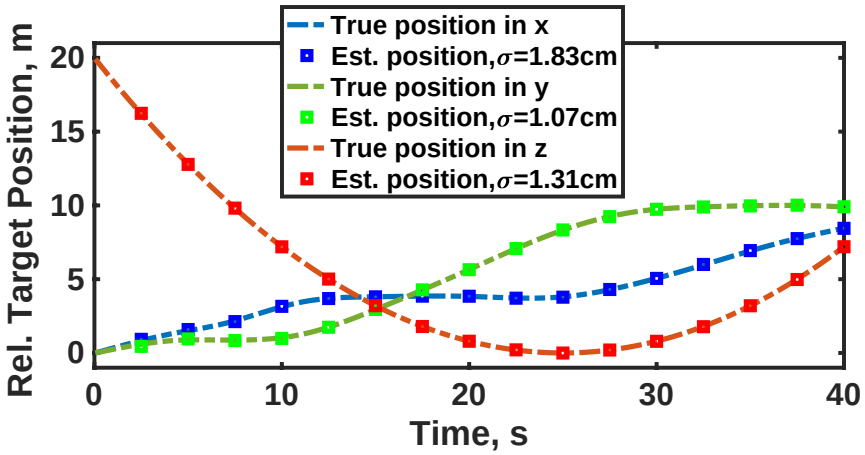

Figure 5.6: True And Estimated Position Of The Aerial Node With Respect To The Ground Node. The EKF Estimates, Indicated Here At Every Measurement Instance, Are Precise Upto 2 Cm In Every Direction.

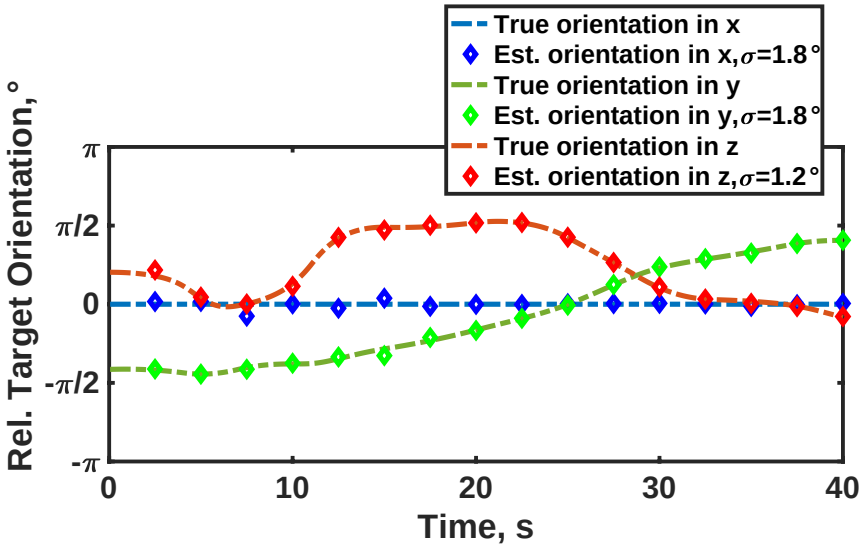

Figure 5.7: True And Estimated Orientation Of The Aerial Node With Respect To The Ground Node. The EKF Estimates, Indicated Here At Every Measurement Instance, Are Precise Upto 2° In Every Direction.

Chapter 6

DYNAMIC SPECTRUM ACCESS

Spectral congestion limits the opportunities and performance of radio frequency (RF) systems. Spectral isolation sufficiently mitigates this congestion for a small number of users but does not offer a scalable solution once the entire spectrum is occupied. Dynamic resource management supports higher user densities by constantly renegotiating spectral access depending on need and opportunity. This approach promises efficient spectral access but is predicated on cooperation between different types of RF systems, which is a significant paradigm shift for many legacy technologies. Intelligent transportation systems (ITS) rely on several different types of RF services such as radar, communications, and positioning, navigation, and timing (PNT). RF Convergence demonstrates that many of these systems can be executed simultaneously using efficient cooperation strategies, which improves performance and limits spectral access. In this study, we demonstrate a simultaneous positioning, navigation, timing, and communications system that cooperatively executes multiple RF services. We define a "constant-information ranging" strategy that maintains constant information learned about an incoherent moving target by modulating the revisit interval to minimize the number of interactions. This significantly reduces spectral congestion and offers a control mechanism to dynamically manage spectral access. We validate the constant-information ranging algorithm in a simulation environment where we observe a 91% reduction in spectral access for a particular flight path while maintaining a 3 cm precision in ranging. Results and formulation in this chapter are published in

[25]. Another approach to allocate spectrum dynamically is presented in [26].

6.1 Motivation

Spectral congestion limits the opportunities and performance of radio frequency (RF) systems. Every RF device must share limited spectral resources, which becomes increasingly challenging as we continue to introduce more devices into congested environments. Spectral isolation offered sufficient interference mitigation in the past, but now that every spectrum allocation is filled it doesn't provide a scalable solution for adding more devices.

Modern RF technologies must be supported by efficient resource management strategies and cooperation techniques to overcome spectral congestion. RF Convergence is a growing field of cooperative design techniques that enable significant performance and efficiency enhancements for a broad range of RF systems [1]. Many of these techniques promise significantly lesser resource consumption [2, 3], but they also require cooperation between different types of RF applications. We have previously demonstrated that these techniques offer feasible solutions for many types of RF systems [9, 71, 72], but they require a significant paradigm shift from traditional system design techniques.

Intelligent transport systems (ITS) are increasingly popular, promising unprecedented transportation safety and efficiency. These systems, however, require several simultaneous RF services such as radar, communications, and positioning, navigation, and timing (PNT). This significantly increases spectral congestion, especially as more vehicles begin to adopt these systems.

To address spectral congestion in the context of ITS, we developed the Communications and High-Precision Positioning (CHP2) system to simultaneously provide positioning, navigation, timing, and communications services to cooperative RF users

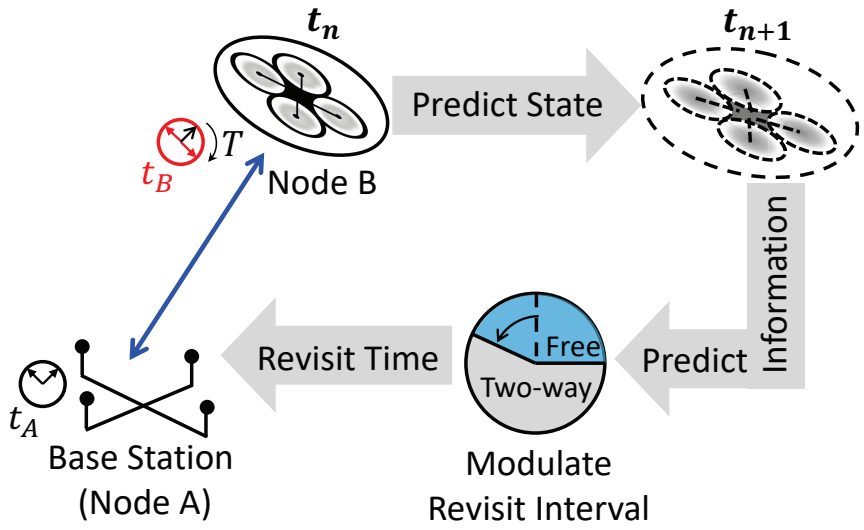

Figure 6.1: System Diagram Of The Constant-Information Ranging Algorithm. A Base-Station A Tracks An Aerial User B. Based On Previous Measurements, The Base Station Predicts The Position Of User B During The Next Measurement State. Depending On How Well User A Can Predict The Path Of User B, We Can Modulate How Often A Measurement Occurs To Maintain A Constant Information Rate. If The Path Is Perfectly Predictable, No Information Is Learned By Taking Additional Measurements, So We Can Divert Spectral Resources To Other Uses.

[9, 18–20]. CHP2 is a two-way ranging (TWR) system that adopts many RF Convergence design techniques to limit spectral access while providing higher precision (<10 cm) with limited bandwidth (10 MHz) and better security than alternatives such as GPS.

In this chapter, we extend this result by developing a "constant-information ranging" (CIR) protocol. This algorithm dynamically reduces spectral access by modulating how often a moving target is measured. CIR quantifies the amount of information learned during each interaction and adjusts the revisit interval to maintain a constant information rate; if a target is moving in a predictable manner, we can reduce the

number of interactions while maintaining the ranging precision. This reduces the spectral access of the system, which reduces the overall spectral congestion and allows other devices to operate more often. This addresses many of the issues associated with fixed resource allocation in RF networks and readily supports dynamic spectrum access techniques in the context of ITS.

6.2 Prior Work and Contributions

CHP2 [18] is a two-way ranging (TWR) system that simultaneously synchronizes distributed clocks and estimates ToF [4, 20, 53] between users. The constant-information ranging algorithm builds upon previous results for radar-based tracking [73–75]. RF Convergence often considers systems with different performance metrics that are difficult to compare. The "estimation rate" was proposed in [76] as an information theory metric that was compatible with systems traditionally dominated by estimation theory (radar, for example). This metric captures the amount of information learned by a given measurement [3, 77, 78], and is particularly useful when trying to dynamically allocate spectral resources between different kinds of systems, such as radar and communications [79, 80]. In this chapter, we make the following contributions to the CHP2 system

- Propose a novel, constant-information ranging algorithm that dynamically reduces spectral access by optimizing the revisit time for a moving target
- Demonstrate that the CIR algorithm significantly reduces spectral access for particular flight paths in simulation.

6.3 Revisit Time Modulation

The original CHP2 system operates using fixed transmission intervals. In many scenarios, however, a user may move very predictably, so each measurement does not yield very much new information. In this scenario, taking measurements at fixed intervals is redundant and wastes spectral resources.

We can reduce spectral congestion by modulating the revisit interval to only take a measurement when it will yield significant information about the target. By focusing on maintaining a constant information learned about the target, we can reduce the number of transmissions, thereby opening the spectrum for other uses. We leverage multiple hypothesis testing to predict and sustain a constant information rate accumulated by each measurement.

For a given scenario, we define a constant information rate I_{const} that we intend to maintain. After each cycle, we allow some processing time t_p and consider a set of potential revisit times t_r^m, $\forall\ m \in \{1, 2, \cdots, M\}$. The potential cycle lengths become

$$L_A^{m,(n-1)} = (t_{A,Rx}^{(n-2)} - t_{A,Tx}^{(n-3)}) + t_p + t_r^m. \tag{6.1}$$

For each potential revisit time, we predict the quantity of information attained by conducting a measurement and choose the cycle length that most closely matches the constant information constraint, i.e.

$$L_A^{(n-1)} \ = \ \mathrm{argmin}_{L_A^{m,(n-1)}} \left| \mathrm{I}^{m,(n-1)} - \mathrm{I}_{const} \right|, \tag{6.2}$$

where $|\cdot|$ is the absolute operator and $\mathrm{I}^{m,(n-1)}$ is the predicted information gained from a measurement at time t_r^m, calculated using (6.6). Given this choice, user A instigates the next transmission at time

$$t_{A,Tx}^{(n-1)} \ = \ t_{A,Tx}^{(n-3)} + L_A^{(n-1)} \tag{6.3}$$

and executes the Kalman Filter tracking methodology defined in Algorithm 2.

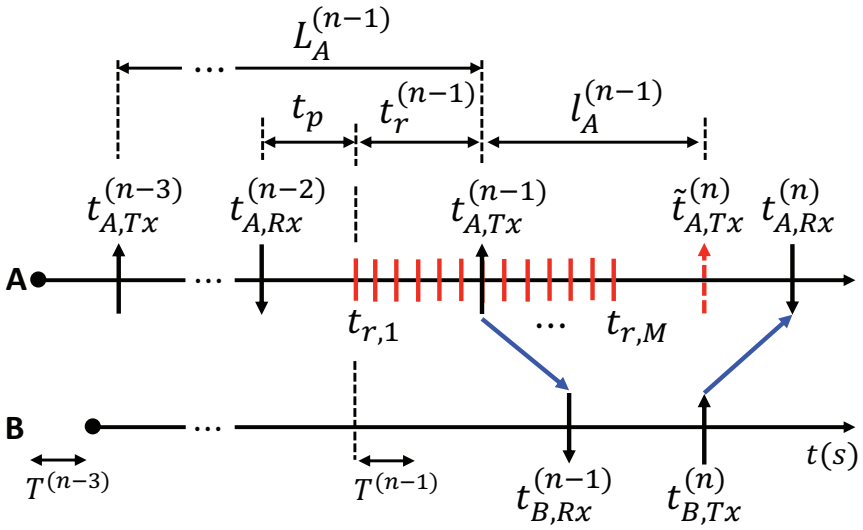

Figure 6.2: Updated Timing Exchange Model Including Processing Time t_p And Dynamic Revisit Time t_r. We Consider Multiple Choices For t_r And Choose The One That Most Closely Matched The Information Constraint I_{const}. This Allows The System To Modulate The Revisit Time And Dynamically Reduce Spectral Access When The Target Behaves Predictably.

6.3.1 Estimation Rate

Estimation rate quantifies the rate of information gained by subsequent measurements of a target [76]. Under a Gaussian assumption, the estimation rate is given by [3, 73]

$$\mathrm{R}_{\mathrm{est}} \leq \frac{1}{2\,t} \log_2\left(\frac{\sigma^2_{\mathrm{proc}} + \sigma^2_{\mathrm{est}}}{\sigma^2_{\mathrm{est}}}\right), \tag{6.4}$$

where σ^2_{proc} and σ^2_{est} are the process and estimation noise variances and t is the measurement interval.

In the context of CHP2, the predicted estimation rate is

$$\mathrm{R}^{m,(n-1)}_{\mathrm{est}} \leq \frac{1}{2\,L_A^{m,(n-1)}} \log_2\left(\frac{|\,\mathbf{S}^{(n-1)}\,|}{|\,\mathbf{R}^{(n-1)}\,|}\right), \tag{6.5}$$

where $L_A^{m,(n-1)}$ is the m^{th} hypothetical cycle length and $|\cdot|$ is a determinant operator. $\mathbf{S}^{(n-1)} = \mathbf{H}^{(n-1)}\mathbf{Q}^{(n-1)}\mathbf{H}^{(n-1)^T} + \mathbf{R}^{(n-1)}$ is a combination of the estimation noise covariance matrix $\mathbf{R}$ and the process noise covariance matrix $\mathbf{Q}$ projected onto the measurement space via the Jacobian $\mathbf{H}$. The estimation rate may be interpreted as the minimum number of bits needed to encode the Kalman residual. The predicted information is then written as a function of m such that

$$\mathrm{I}^{m,(n-1)} = \frac{1}{2}\log_2\left(\frac{|\,\mathbf{S}^{(n-1)}\,|}{|\,\mathbf{R}^{(n-1)}\,|}\right). \tag{6.6}$$

This quantity is a function of the cycle length, so modulating the revisit time will directly change the amount of information gained by a given measurement.

6.4 Simulations

We demonstrate that the constant-information ranging (CIR) protocol significantly reduces spectral access compared to a fixed interval protocol in the context of CHP2. We simulated a stationary, ground user A and a mobile, airborne user B following an arbitrary flight path (Figure 6.3). The relative time-of-flight and radial velocity between these two nodes are depicted in Figure 6.4. The relative clock offset and drift are modeled using realistic oscillator characteristics, shown in Figure 6.5.

We assume that the state and measurement noise covariance matrices are known *a priori*. These may be adaptively estimated in real time but this discussion is beyond the scope of this report. We model these matrices as a function of integrated SNR to fit the flight trajectory. CHP2 operates with 30 dB of waveform integration gain and maintains an operational instantaneous SNR of 15 dB, which yields ToA estimates precise to within 0.1 ns (3 cm) [9].

We define a constant information rate $\mathrm{I}_{const} = 15$ bits, processing time $t_p = 30$ ms, and construct a lattice of revisit time hypotheses t_r^m between 0 and 2 s with a

Algorithm 2 Constant Information Ranging Protocol

while true **do**

$L_A^{m,(n-1)} \in \{L_A^{1,(n-1)},\ L_A^{2,(n-1)},\ \cdots,\ L_A^{M,(n-1)}\}$

for $m = 1 : M$ **do**

$\hat{\mathbf{x}}_{(-)}^{(n-1)} = \mathbf{F}(L_A^{m,(n-1)})\,\hat{\mathbf{x}}^{(n-3)}$

$\hat{\mathbf{P}}_{(-)}^{(n-1)} = \mathbf{F}^{(n-1)}\hat{\mathbf{P}}^{(n-3)}\mathbf{F}^{(n-1)^T} + \mathbf{Q}^{(n-1)}$

$\mathbf{H}^{(n-1)} = \frac{\partial \mathbf{h}(\hat{\mathbf{x}})}{\partial \hat{\mathbf{x}}}\Big|_{\hat{\mathbf{x}}_{(-)}^{(n-1)}}$

$\mathbf{S}^{(n-1)} = \mathbf{H}^{(n-1)}\hat{\mathbf{P}}_{(-)}^{(n-1)}\mathbf{H}^{(n-1)^T} + \mathbf{R}^{(n-1)}$

$\mathrm{I}^{m,(n-1)} = \frac{1}{2}\log_2\left(\left|\,\mathbf{S}^{(n-1)}\,\right|/\left|\,\mathbf{R}^{(n-1)}\,\right|\right)$

end

$L_A^{(n-1)} = \mathrm{argmin}_{L_A^{m,(n-1)}}\left|\mathrm{I}^{m,(n-1)} - \mathrm{I}_{const}\right|$

$t_{A,Tx}^{(n-1)} = t_{A,Tx}^{(n-3)} + L_A^{(n-1)}$, conduct two-way timing exchange

$\hat{\mathbf{z}}_{(-)}^{(n-1)} = \mathbf{u}^{(n-1)} + \mathbf{h}(\hat{\mathbf{x}}_{(-)}^{(n-1)})$

$\mathbf{K}^{(n-1)} = \hat{\mathbf{P}}_{(-)}^{(n-1)}\mathbf{H}^{(n-1)^T}\mathbf{S}^{(n-1)^{-1}}$

$\hat{\mathbf{x}}^{(n-1)} = \hat{\mathbf{x}}_{(-)}^{(n-1)} + \mathbf{K}^{(n-1)}(\mathbf{z}^{(n-1)} - \hat{\mathbf{z}}_{(-)}^{(n-1)})$

$\hat{\mathbf{P}}^{(n-1)} = (\mathbf{I}_{|\mathbf{x}|} - \mathbf{K}^{(n-1)}\mathbf{H}^{(n-1)})\hat{\mathbf{P}}_{(-)}^{(n-1)}$

end

resolution of 5 ms.We simulate this scenario for 60 seconds, during which a traditional CHP2 user would ordinarily transmit a joint positioning-communications waveform every 100 ms for a total of 600 measurements.

We implement the CIR protocol defined by Algorithm 1 given these parameters and plot the optimal revisit times in Figure 6.6. To maintain the 15 bit information constraint, the revisit interval is increased from 100 ms to over 1 second, resulting in only 50 measurements in the same 60 second time frame. This reduces the spectral usage by over 91% for the flight path depicted in Figure 6.3. Despite the drastic reduction in spectral resources, CHP2 maintains a 3 cm precision in ranging

and synchronizing clocks upto 0.08 ns, see Figures 6.4 and 6.5. These figures also demonstrates that as the target exhibits less predictable behavior (during the curve vs. straight line), user A measures user B more often because the behavior is more divergent from the prediction so there is more information to be gained by taking a measurement.

6.5 Summary

Spectral congestion limits the opportunities and performance of radio frequency (RF) systems. We developed the Communications and High-Precision Positioning (CHP2) system to simultaneously enable network communications and relative localization for intelligent transport systems (ITS). By adopting RF Convergence co-design techniques, this system executes high-precision ranging (< 10 cm) with limited spectral access (10 MHz). We proposed a constant-information ranging (CIR) technique

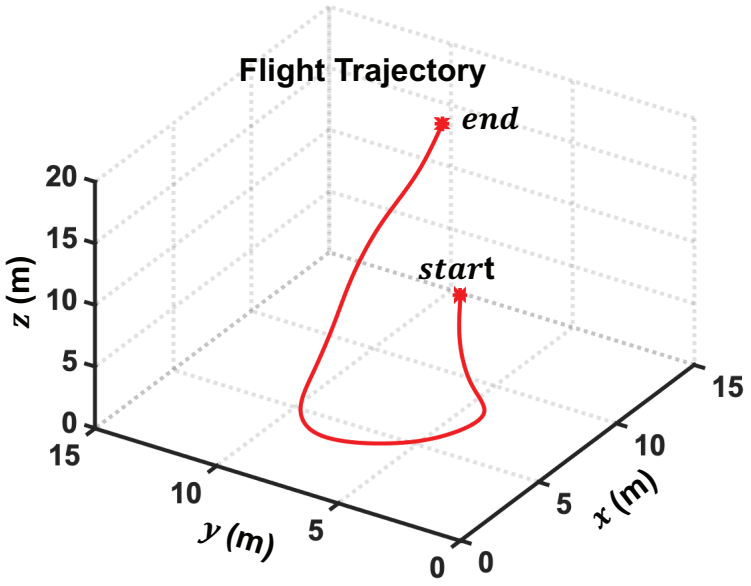

Figure 6.3: Simulated Flight Trajectory Of User B For 60 Seconds. User A Is Stationary, Situated At The Origin.

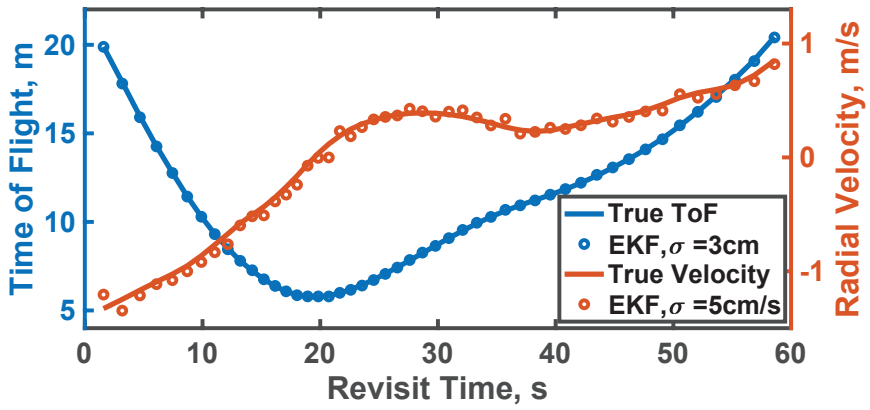

Figure 6.4: True And Estimated Relative Time-Of-Flight (ToF) And Radial Velocity Between The Two Users. The EKF Estimates, Indicated Here At Every Measurement Instance, Are Precise Upto 3 Cm And 5 Cm/s Respectively. When The Target's Flight Path Diverges From Predictions (During The Curve Vs. Straight Line) The Frequency Of Measurements Increases.

to further reduce spectral access for this class of two-way ranging (TWR) systems. This algorithm dynamically optimizes the revisit interval to minimize the number of interactions while maintaining a constant information rate, thereby reducing the spectral usage. CIR negotiates dynamic spectrum access within a CHP2/TWR network but also provides an interface for other dynamic spectrum access techniques. In a MATLAB simulation environment, we demonstrated a 91% reduction in spectral usage given a set of reasonable operating conditions and flight trajectory while maintaining a 3 cm precision in ranging and 0.08 ns precision in clock sync.

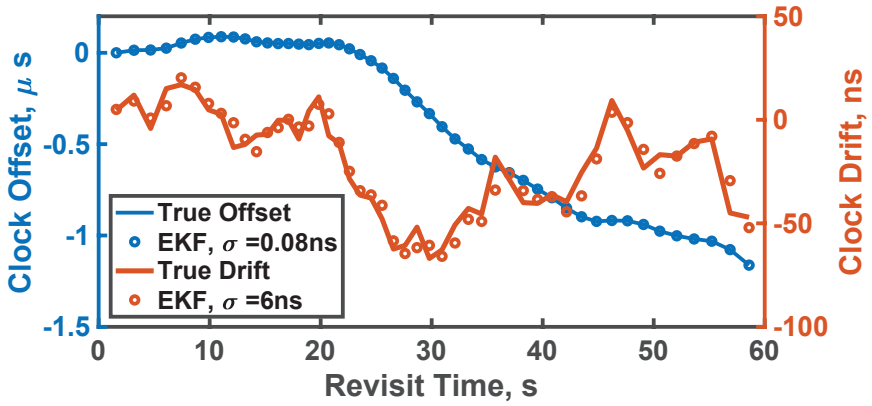

Figure 6.5: True And Estimated Relative Clock Offset And Drift Between The Two Users. The EKF Estimates Are Precise Upto 0.08 Ns And 6 Ns Respectively. When The Relative Clock Behavior Diverges From The Model (During The Curve Vs. Straight Line) Measurements Occur More Often.

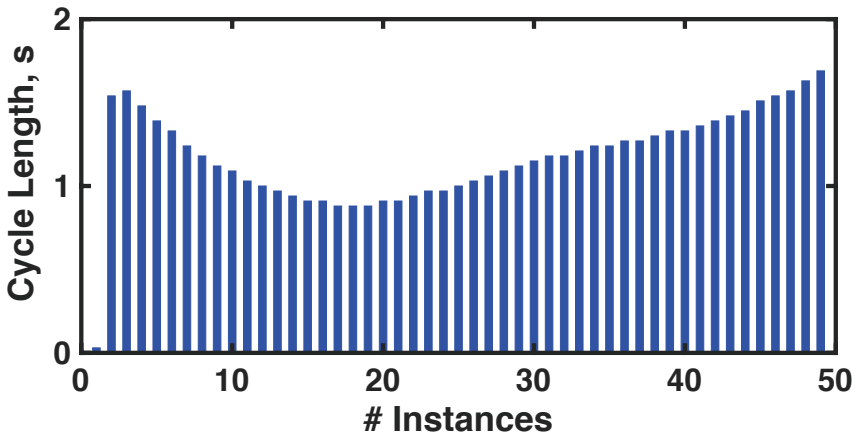

Figure 6.6: Optimal Cycle Length To Maintain A Constant Information Of 15 Bits At Each Measurement Instance. In This Example, Using CIR To Modulate The Revisit Time Reduces Spectral Usage By Over 91%.

Chapter 7

EXPERIMENTAL RESULTS

7.1 COTS Experimental Testbed

We deployed CHP2 on a commercial-off-the-shelf (COTS) radio hardware platform. We briefly describe this experimental testbed and discuss system performance for the algorithms described above. The CHP2 system operates at a center frequency of 915 MHz in the U.S. (783 MHz in Europe) with 10 MHz bandwidth. We deployed two CHP2 testbeds like the one pictured in Figure 7.1. These users execute the aforementioned timing exchange over 4 custom-built, omni-directional antennae with a gain of 3 dBi. On each testbed, signal processing is executed by the motherboard (Xilinx ZCU102) and communications are enabled by an RF front end transceiver card (ADI FMCOMMS5) in conjunction with a customized transmit-receive (TR) switching amplifier board. A slew of supporting hardware like a battery pack, power supply modules and antenna bolstering structures are mounted onto an aluminum frame. The antenna mounts are designed and 3D printed to uniquely fit the frame and are configured to be detachable. This enables rapid reconfiguration to change the form factor of the unit, allowing the antenna placements to be changed.

7.2 Cabled Tests

To allow for a controlled test, two of the experimental testbeds are connected via RF cables to form a 4×4 cabled link. These two users alternate transmitting and receiving timing information for 70 seconds via the joint positioning-communications waveform. The ToA of these interactions are estimated via the interpolated massive

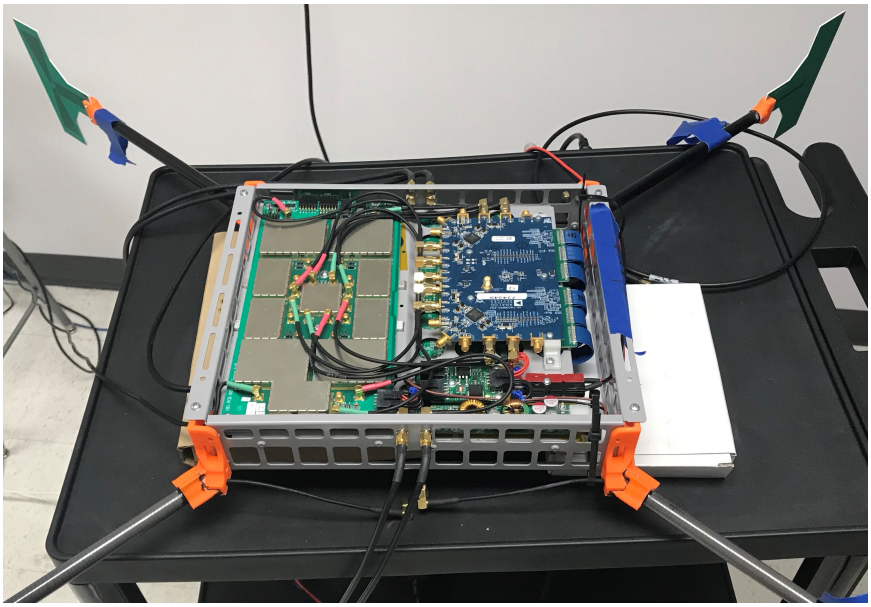

Figure 7.1: COTS Experimental Hardware Mounted In An Aluminum Frame. The Amplifier And Transmit-Receive Switching Board (Left) Is Shielded With Modular Copper Plating. The RF Board (Blue, Right) Sits On Top Of The Motherboard Underneath. The Antennas (Top Left And Right) Are Mounted To Carbon Fiber Tubes Through Which RF Feeds Are Fed And Connected To The Amplifier Board.

correlator technique whose performance, as a function of operating SNR, is presented in Figure **??**. The ToA estimates in conjunction with information accrued via the two-way cooperative exchange fuels a variety of joint clock synchronization and ToF estimation techniques. We measure the performance of a few of these estimators, defined in Section **??**, in terms of ranging precision. We subtract the mean from these ToF estimates to highlight the improvement in precision. These results are plotted in Figures 7.2, 7.3 and 7.4.

The timestamps are processed by the deterministic estimators HTP and STP are both unbiased and provide ranging accuracy of 2.64 cm and 2.03 cm respectively. STP is a one-shot estimator and optimal whereas HTP is iterative hence also compu-

tationally expensive. The filtering methods Extended and Unscented Kalman filters are Bayesian tracking techniques that offer sub-centimeter precision in ToF estima-

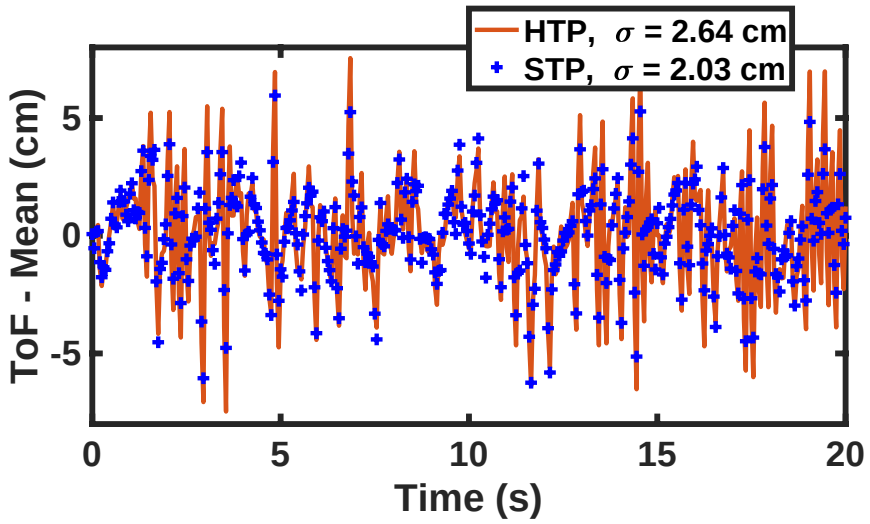

Figure 7.2: ToF Estimates Minus Mean, After Applying Deterministic Estimators HTP And STP. Both The Algorithms Perform Comparably, Maintaining A Ranging Standard Deviation Of Less Than 3 Cm.

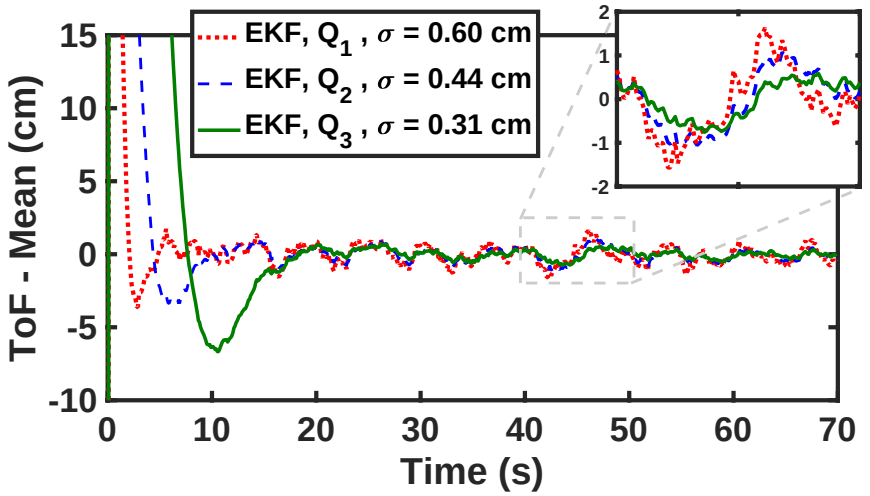

Figure 7.3: ToF Estimates Minus Mean, After Applying Adaptive Extended Kalman Filters (AEKF). Adjusting The Initial Q Estimate Decreases The Observed Standard Deviation But Also Increases The Settling Time.

tion. We opt for residual-based adaptive noise covariance evaluation that assists in adapting to changing flight paths and relative clock offsets. These filtering methods drive a trade-off between speed and accuracy of convergence. This is evident from Figures 7.3 and 7.4. When we seed the AEKF tracking with three different initial process noise covariance matrices Q_1, Q_2 and Q_3, the ranging estimates are precise to within 0.60 cm, 0.44 cm and 0.31 cm while the time to converge increases as 5 s, 10 s and 20 s respectively. Similarly, AUKF filters demonstrate precision in ToF estimates upto 0.63 cm, 0.48 cm and 0.34 cm while the taking 8 s, 15 s, 35 s to converge. While Adaptive EKF (AEKF) offer slightly better performance, the Adaptive UKF method is more robust to non-linear flight paths and requires lower mathematical computations for higher order Markov model assumptions.

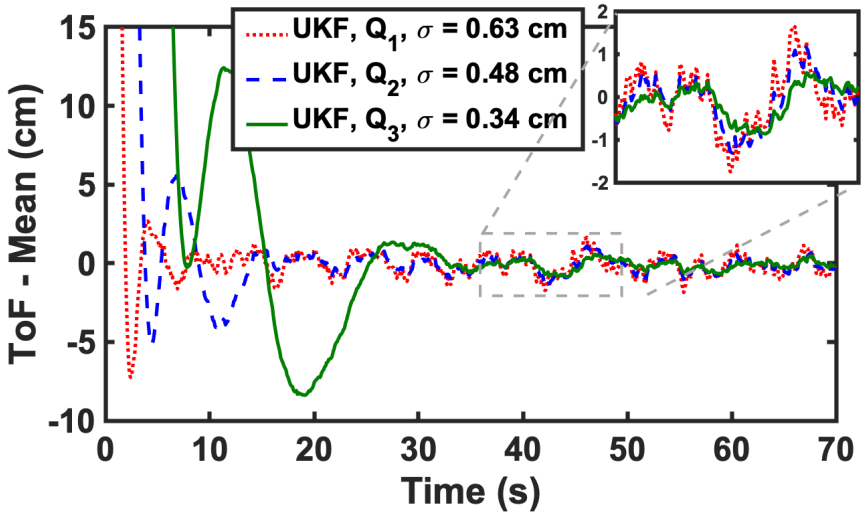

Figure 7.4: ToF Estimates Minus Mean, After Applying Adaptive Unscented Kalman Filters (AUKF). Adjusting The Initial Q Estimate Decreases The Observed Standard Deviation But Also Increases The Settling Time.

7.3 Summary

In this chapter, we demonstrate the ranging capabilities of the Communications and High-Precision Positioning (CHP2) system using several ToF algorithms. We demonstrate that this system supports sub-cm ranging precision with 10 MHz bandwidth. We compare iterative and "one-shot" techniques to an Adaptive Extended Kalman filter (AEKF) and an Unscented Kalman filter (UKF). We observe that the AEKF solution converges faster and achieves slightly better ranging performance, but the UKF is more robust to non-linear flight paths and higher order Markov model mismatch. Both filtering techniques outperformed the original estimators by nearly an order of magnitude at the cost of some settling time. Due to the integrated communications component of this system, it is naturally robust to spoofing and hijacking cyberattacks that broadcast techniques such as GPS are especially vulnerable to. Furthermore, CHP2 simultaneously enables network communications and distributed time synchronization for users using consumer-grade local oscillators in a relatively narrow spectral allocation. Thus, we assert that CHP2 is a suitable candidate for CNS and PNT services for safety-critical air transport systems.

Chapter 8

SUMMARY AND FUTURE WORK

8.1 Future Work

Complement Legacy Systems Previous chapters in this report have demonstrated the use of communications channel to position an a CHP2 node relative to another. Often, however, information from a single 'sensor' might be insufficient to achieve hyper precise positioning. This is when an array of sensors available on board an airborne platform can be used to improve accuracy in tracking it. Two such sensors are IMU and GPS.

Inertial Measurement Unit (IMU) An IMU comprises of an accelerometer, gyro and magnetometer for each axis of rotation of the assumed reference so-ordinate system. With the aid of these gauges, it detects linear acceleration, rotational rate and a heading reference respectively. However these measurements are erroneous and drift in time. One of the sources of these errors is bias in the sensor readings are accumulative when not corrected for regularly and hence add up in time. An IMU is mounted on an aircraft and the axis of this navigation aid needs to be in perfect alignment with the axis if the aircraftâĂŹs body. When the body axis is misaligned with respect to the IMUâĂŹs reference frame, it induces errors in the measurements.

Global Positioning System (GPS) Since 1995, aircraft tracking systems utilize GPS to locate the vehicle with respect to a fleet of navigation satellites. A set of 24 satellites in orbit, constantly transmit their geolocation and clock information maintained by atomic clocks. A GPS receiver solves equations to determine its precise position and deviation from true time, based on these inputs. However GPS

necessitates a line of sight between the satellites and 53 the receiver. Therefore with environments prone to multipath, GPS produces errors about hundreds of meters. Also, at every instant of time, a receiver needs to be in LOS with at least 4 satellites. When a receiver moves between cells of coverage, the switching procedure causes erroneous readings.

Simultaneous Communications and Positioning This report focused on a method of positioning with the aid of communications be- tween the aircraft and ground node. This algorithm has a potential to produce pre- cise position and orientation estimates but is limited by LOS between the two nodes. Like GPS, a multipath environment can be a major source of error for this algorithm. Also, communication link is a crucial part of the proposed algorithm that makes tim- ing exchange mechanism possible. Hence its reliability is the key in attaining precise estimates. An unreliable communication link with poor channel estimation capability, low SNR of operation, bad coding schemes all effect the precision of estimation.

Sensor Fusion We can see that any one positioning system is inefficient in generating precise position and orientation (POSE) estimates consistently. They are bound to fail in different regime of operation. To be able to maintain consistent performance in POSE detection and tracking, a fusion of these sensor information can be attempted. First, the three sensor data is translated into a set of common position and orientation measurements. This can be done by translating IMUs velocities to a reference frame using rotation matrices. Assuming location of monitoring ground node is known, SCPs measurements can be transformed to the same reference frame. A Kalman filter can now track the aircraft by combining the measurements from GPS, translated sensor reading from IMU and SCP.

Effect of Multipath and Shadowing During flight a few of the antennae are obstructed by the structure of the UAV. signal received at this antenna is either not

a result of los or diffraction. SNR of the signal is week and the estimates from this antenna are disruptive to tracking the center of mass. Propose a method to eliminate bad measurements using measured SNR. Such adaptive tracking aids in protecting precision in positioning.

In wireless communications, fading is variation of the attenuation of a signal with various variables. These variables include time, geographical position, and radio frequency. Fading is often modeled as a random process. A fading channel is a communication channel that experiences fading. In wireless systems, fading may either be due to multipath propagation, referred to as multipath-induced fading, weather (particularly rain), or shadowing from obstacles affecting the wave propagation, sometimes referred to as shadow fading.

The presence of reflectors in the environment surrounding a transmitter and receiver create multiple paths that a transmitted signal can traverse. As a result, the receiver sees the superposition of multiple copies of the transmitted signal, each traversing a different path. Each signal copy will experience differences in attenuation, delay and phase shift while traveling from the source to the receiver. This can result in either constructive or destructive interference, amplifying or attenuating the signal power seen at the receiver. Strong destructive interference is frequently referred to as a deep fade and may result in temporary failure of communication due to a severe drop in the channel signal-to-noise ratio.

8.2 Summary

Spectral congestion limits the opportunities and performance of radio frequency (RF) systems. We developed the Communications and High-Precision Positioning (CHP2) system to simultaneously enable network communications and relative localization for intelligent transport systems (ITS). By adopting RF Convergence co-design

techniques, this system executes high-precision ranging (< 1 cm) with limited spectral access (10 MHz).

Localization is key for highly adaptive self-organizing *ad hoc* networks. We proposed a family of optimal one-shot methods that jointly achieve distributed coherence and ranging estimation. We recognize that such estimators reduce to a system of linear equations and hence are optimal. We studied through simulations, precision, computational complexity and region of applicability for two of such variants and comment on higher order generalizations and extension to multiple antennae systems.

This inspired reformulating these estimators to enable tracking. We elaborated on two-way ranging methods for jointly track propagation delay and clock offset between the nodes in the network. Kalman Filter (EKF) algorithm under first and second order Markov models was explored. We demonstrate their workings for simulated flight paths, study their performance and identify their region of applicability. We extended this formulation for higher order models on state space parameters and to joint delay-offset estimation in multiple antenna systems.

We then expand on the system capabilities to track position and orientation of target node. In doing so, we put together a novel joint tracking algorithm that is conducive to use with any time-of-arrival based systems. We demonstrate their workings for simulated flight paths and discuss the effect of geometric dilution of precision on precision in positioning.

We proposed a constant-information ranging (CIR) technique to further reduce spectral access for this class of two-way ranging (TWR) systems. This algorithm dynamically optimizes the revisit interval to minimize the number of interactions while maintaining a constant information rate, thereby reducing the spectral usage. CIR negotiates dynamic spectrum access within a CHP2/TWR network but also provides an interface for other dynamic spectrum access techniques. In a MATLAB

simulation environment, we demonstrated a 91% reduction in spectral usage given a set of reasonable operating conditions and flight trajectory while maintaining a 3 cm precision in ranging and 0.08 ns precision in clock sync.

We deployed CHP2 on a commercial-off-the-shelf (COTS) radio hardware platform. The CHP2 system operates at a center frequency of 915 MHz in the U.S. (783 MHz in Europe) with 10 MHz bandwidth. We demonstrate that this system supports sub-cm ranging precision via cabled tests.

REFERENCES

[1] B. Paul, A. R. Chiriyath, and D. W. Bliss, "Survey of rf communications and sensing convergence research," *IEEE Access*, vol. 5, pp. 252–270, 2016.

[2] A. R. Chiriyath, B. Paul, G. M. Jacyna, and D. W. Bliss, "Inner bounds on performance of radar and communications co-existence," *IEEE Transactions on Signal Processing*, vol. 64, no. 2, pp. 464–474, 2015.

[3] A. R. Chiriyath, B. Paul, and D. W. Bliss, "Radar-communications convergence: Coexistence, cooperation, and co-design," *IEEE Transactions on Cognitive Communications and Networking*, vol. 3, no. 1, pp. 1–12, 2017.

[4] P. Bidigare, U. Madhow, R. Mudumbai, and D. Scherber, "Attaining fundamental bounds on timing synchronization," in *2012 IEEE International Conference on Acoustics, Speech and Signal Processing (ICASSP)*. IEEE, 2012, pp. 5229–5232.

[5] P. Bidigare, S. Pruessing, D. Raeman, D. Scherber, U. Madhow, and R. Mudumbai, "Initial over-the-air performance assessment of ranging and clock synchronization using radio frequency signal exchange," in *2012 IEEE Statistical Signal Processing Workshop (SSP)*. IEEE, 2012, pp. 273–276.

[6] T. E. McEwan, "Time-of-flight radio location system," Apr. 23 1996, uS Patent 5,510,800.

[7] L. W. Fullerton, J. L. Richards, and I. A. Cowie, "System and method for position determination by impulse radio using round trip time-of-flight," Aug. 26 2003, uS Patent 6,611,234.

[8] S. Lanzisera, D. Zats, and K. S. Pister, "Radio frequency time-of-flight distance measurement for low-cost wireless sensor localization," *IEEE Sensors Journal*, vol. 11, no. 3, pp. 837–845, 2011.

[9] A. Herschfelt, H. Yu, S. Wu, H. Lee, and D. W. Bliss, "Joint positioning-communications system design: Leveraging phase-accurate time-of-flight estimation and distributed coherence," in *2018 52nd Asilomar Conference on Signals, Systems, and Computers*. IEEE, 2018, pp. 433–437.

[10] D. L. Mills, "Internet time synchronization: the network time protocol," *IEEE Transactions on communications*, vol. 39, no. 10, pp. 1482–1493, 1991.

[11] D. Mills, "Network time protocol (version 3) specification, implementation and analysis," Tech. Rep., 1992.

[12] B. Sundararaman, U. Buy, and A. D. Kshemkalyani, "Clock synchronization for wireless sensor networks: a survey," *Ad hoc networks*, vol. 3, no. 3, pp. 281–323, 2005.

[13] I. Guvenc and C.-C. Chong, "A survey on toa based wireless localization and nlos mitigation techniques," *IEEE Communications Surveys & Tutorials*, vol. 11, no. 3, pp. 107–124, 2009.

[14] W. Navidi, W. S. Murphy Jr, and W. Hereman, "Statistical methods in surveying by trilateration," *Computational statistics & data analysis*, vol. 27, no. 2, pp. 209–227, 1998.

[15] N. Patwari, A. O. Hero, M. Perkins, N. S. Correal, and R. J. O'dea, "Relative location estimation in wireless sensor networks," *IEEE Transactions on signal processing*, vol. 51, no. 8, pp. 2137–2148, 2003.

[16] M. A. Spirito, "On the accuracy of cellular mobile station location estimation," *IEEE Transactions on vehicular technology*, vol. 50, no. 3, pp. 674–685, 2001.

[17] E. J. Lefferts, F. L. Markley, and M. D. Shuster, "Kalman filtering for spacecraft attitude estimation," *Journal of Guidance, Control, and Dynamics*, vol. 5, no. 5, pp. 417–429, 1982.

[18] A. Herschfelt, H. Yu, S. Wu, S. Srinivas, Y. Li, N. Sciammetta, L. Smith, K. Rueger, H. Lee, C. Chakrabarti, and D. W. Bliss, "Joint positioning-communications system design and experimental demonstration," in *2019 IEEE/AIAA 38th Digital Avionics Systems Conference (DASC)*. IEEE, 2019, pp. 1–6.

[19] A. Herschfelt, "Simultaneous positioning and communications: Hybrid radio architecture, estimation techniques, and experimental validation," Ph.D. dissertation, Arizona State University, 2019.

[20] S. Srinivas, A. Herschfelt, and D. W. Bliss, "Joint positioning-communications system: Optimal distributed coherence and positioning estimators," in *2019 53rd Asilomar Conference on Signals, Systems, and Computers*. IEEE, 2019, pp. 317–321.

[21] ——, "Communications and high precision positioning (chp2): Simultaneous distributed coherence and time-of-flight tracking via kalman filtering techniques," *submitted to IEEE Transactions on Aerospace and Electronic systems*, 2021.

[22] J. Echols, S. Srinivas, A. Herschfelt, and D. W. Bliss, "Oscillator colored noise modeling for navigation filtering applications," *submitted to IEEE Transactions on signal processing*, 2021.

[23] S. Srinivas, A. Herschfelt, and D. W. Bliss, "Communications and high-precision positioning (chp2): Joint localization and orientation tracking in multi antenna setup," in *2021 IEEE Aerospace Conference, pending publication*. IEEE, 2021.

[24] ——, "Communications and high-precision positioning (chp2): Cycle slip trellis trimming algorithm," in *2021 IEEE Aerospace Conference, pending publication*. IEEE, 2021.

[25] S. Srinivas, A. Herschfelt, A. Chiriyath, and D. W. Bliss, "Joint positioning-communications: Constant-information ranging for dynamic spectrum access," in *2020 IEEE 91th Vehicular Technology Conference (VTC2020-Fall), pending publication.* IEEE/AIAA, 2020.

[26] O. Ma, A. Herschfelt, H. Yu, S. Wu, S. Srinivas, Y. Li, H. Lee, C. Chakrabarti, and D. W. Bliss, "Communications and high-precision positioning (chp2): Secure traffic and resource management using reinforcement learning," in *39th Digital Avionics Systems Conference (DASC), pending publication.* IEEE/AIAA, 2020.

[27] S. Srinivas, A. Herschfelt, H. Yu, S. Wu, Y. Li, H. Lee, C. Chakrabarti, and D. W. Bliss, "Communications and high-precision positioning (chp2): Enabling secure cns and apnt for safety-critical air transport systems," in *39th Digital Avionics Systems Conference (DASC), pending publication.* IEEE/AIAA, 2020.

[28] H. Yu, A. Herschfelt, Y. Li, S. Srinivas, S. Wu, N. Sciammetta, L. Smith, K. Rueger, H. Lee, C. Chakrabarti, and D. W. Bliss, "Communications and high precision positioning (chp2): Hardware architecture, implementation, and experimental validation," *submitted to IEEE Transactions on Vehicular Technology*, 2020.

[29] C. A. Balanis, *Antenna theory: analysis and design.* John wiley & sons, 2016.

[30] D. W. Bliss and S. Govindasamy, *Adaptive wireless communications: MIMO channels and networks.* Cambridge University Press, 2013.

[31] A. Weiss and E. Weinstein, "Fundamental limitations in passive time delay estimation–part i: Narrow-band systems," *IEEE Transactions on Acoustics, Speech, and Signal Processing*, vol. 31, no. 2, pp. 472–486, 1983.

[32] E. Weinstein and A. Weiss, "Fundamental limitations in passive time-delay estimation–part ii: Wide-band systems," *IEEE transactions on acoustics, speech, and signal processing*, vol. 32, no. 5, pp. 1064–1078, 1984.

[33] H. Liu, H. Darabi, P. Banerjee, and J. Liu, "Survey of wireless indoor positioning techniques and systems," *IEEE Transactions on Systems, Man, and Cybernetics, Part C (Applications and Reviews)*, vol. 37, no. 6, pp. 1067–1080, 2007.

[34] Q. Li and D. Rus, "Global clock synchronization in sensor networks," *IEEE Transactions on computers*, vol. 55, no. 2, pp. 214–226, 2006.

[35] M. Pelka, D. Amann, M. Cimdins, and H. Hellbriick, "Evaluation of time-based ranging methods: Does the choice matter?" in *2017 14th Workshop on Positioning, Navigation and Communications (WPNC).* IEEE, 2017, pp. 1–6.

[36] H. Kim, "Double-sided two-way ranging algorithm to reduce ranging time," *IEEE Communications letters*, vol. 13, no. 7, pp. 486–488, 2009.

[37] D.-G. Oh, S.-H. Yoon, and J.-W. Chong, "A novel time delay estimation using chirp signals robust to sampling frequency offset for a ranging system," *IEEE Communications letters*, vol. 14, no. 5, pp. 450–452, 2010.

[38] B. Denis, J.-B. Pierrot, and C. Abou-Rjeily, "Joint distributed synchronization and positioning in uwb ad hoc networks using toa," *IEEE transactions on microwave theory and techniques*, vol. 54, no. 4, pp. 1896–1911, 2006.

[39] A. H. Sayed, A. Tarighat, and N. Khajehnouri, "Network-based wireless location: challenges faced in developing techniques for accurate wireless location information," *IEEE signal processing magazine*, vol. 22, no. 4, pp. 24–40, 2005.

[40] F. Gustafsson and F. Gunnarsson, "Mobile positioning using wireless networks: possibilities and fundamental limitations based on available wireless network measurements," *IEEE Signal processing magazine*, vol. 22, no. 4, pp. 41–53, 2005.

[41] S. Gezici, "A survey on wireless position estimation," *Wireless personal communications*, vol. 44, no. 3, pp. 263–282, 2008.

[42] N. Patwari, J. N. Ash, S. Kyperountas, A. O. Hero, R. L. Moses, and N. S. Correal, "Locating the nodes: cooperative localization in wireless sensor networks," *IEEE Signal processing magazine*, vol. 22, no. 4, pp. 54–69, 2005.

[43] A. Mesmoudi, M. Feham, and N. Labraoui, "Wireless sensor networks localization algorithms: a comprehensive survey," *arXiv preprint arXiv:1312.4082*, 2013.

[44] W. Lewandowski and C. Thomas, "Gps time transfer," *Proceedings of the IEEE*, vol. 79, no. 7, pp. 991–1000, 1991.

[45] W. Lewandowski, J. Azoubib, and W. J. Klepczynski, "Gps: Primary tool for time transfer," *Proceedings of the IEEE*, vol. 87, no. 1, pp. 163–172, 1999.

[46] F. Sivrikaya and B. Yener, "Time synchronization in sensor networks: a survey," *IEEE network*, vol. 18, no. 4, pp. 45–50, 2004.

[47] S. Ganeriwal, R. Kumar, and M. B. Srivastava, "Timing-sync protocol for sensor networks," in *Proceedings of the 1st international conference on Embedded networked sensor systems*, 2003, pp. 138–149.

[48] L. Schenato and G. Gamba, "A distributed consensus protocol for clock synchronization in wireless sensor network," in *2007 46th IEEE Conference on Decision and Control*. IEEE, 2007, pp. 2289–2294.

[49] M. K. Maggs, S. G. O'keefe, and D. V. Thiel, "Consensus clock synchronization for wireless sensor networks," *IEEE sensors Journal*, vol. 12, no. 6, pp. 2269–2277, 2012.

[50] J. Eidson and K. Lee, "Ieee 1588 standard for a precision clock synchronization protocol for networked measurement and control systems," in *Sensors for Industry Conference, 2002. 2nd ISA/IEEE*, vol. 10. Ieee, 2002.

[51] M. L. Sichitiu and C. Veerarittiphan, "Simple, accurate time synchronization for wireless sensor networks," in *2003 IEEE Wireless Communications and Networking, 2003. WCNC 2003.*, vol. 2. IEEE, 2003, pp. 1266–1273.

[52] J. Van Greunen and J. Rabaey, "Lightweight time synchronization for sensor networks," in *Proceedings of the 2nd ACM international conference on Wireless sensor networks and applications*, 2003, pp. 11–19.

[53] D. R. Brown III, A. G. Klein, and R. Wang, "Non-hierarchical clock synchronization for wireless sensor networks," *arXiv preprint arXiv:1212.1216*, 2012.

[54] R. D. Preuss and D. R. Brown, "Retrodirective distributed transmit beamforming with two-way source synchronization," in *2010 44th Annual Conference on Information Sciences and Systems (CISS)*. IEEE, 2010, pp. 1–6.

[55] D. R. Brown and A. G. Klein, "Precise timestamp-free network synchronization," in *2013 47th Annual Conference on Information Sciences and Systems (CISS)*. IEEE, 2013, pp. 1–6.

[56] A. Gelb, *Applied optimal estimation*. MIT press, 1974.

[57] B. D. Anderson and J. B. Moore, *Optimal filtering*. Courier Corporation, 2012.

[58] R. E. Kalman, "A new approach to linear filtering and prediction problems," 1960.

[59] L. Galleani and P. Tavella, "The characterization of clock behavior with the dynamic allan variance," in *IEEE International Frequency Control Symposium and PDA Exhibition Jointly with the 17th European Frequency and Time Forum, 2003. Proceedings of the 2003*. IEEE, 2003, pp. 239–244.

[60] C. Zucca and P. Tavella, "The clock model and its relationship with the allan and related variances," *IEEE transactions on ultrasonics, ferroelectrics, and frequency control*, vol. 52, no. 2, pp. 289–296, 2005.

[61] C. A. Greenhall, "Forming stable timescales from the jones–tryon kalman filter," *Metrologia*, vol. 40, no. 3, p. S335, 2003.

[62] G. Giorgi and C. Narduzzi, "Performance analysis of kalman-filter-based clock synchronization in ieee 1588 networks," *IEEE transactions on instrumentation and measurement*, vol. 60, no. 8, pp. 2902–2909, 2011.

[63] X. R. Li and V. P. Jilkov, "Survey of maneuvering target tracking. part i. dynamic models," *IEEE Transactions on aerospace and electronic systems*, vol. 39, no. 4, pp. 1333–1364, 2003.

[64] L. Galleani, "A tutorial on the two-state model of the atomic clock noise," *Metrologia*, vol. 45, no. 6, p. S175, 2008.

[65] J. A. Davis, C. Greenhall, and P. Stacey, "A kalman filter clock algorithm for use in the presence of flicker frequency modulation noise," *Metrologia*, vol. 42, no. 1, p. 1, 2005.

[66] J. Rutman, "Characterization of phase and frequency instabilities in precision frequency sources: Fifteen years of progress," *Proceedings of the IEEE*, vol. 66, no. 9, pp. 1048–1075, 1978.

[67] D. B. Percival, "Stochastic models and statistical analysis for clock noise," *Metrologia*, vol. 40, no. 3, p. S289, 2003.

[68] Y.-T. Chan, W.-Y. Tsui, H.-C. So, and P.-c. Ching, "Time-of-arrival based localization under nlos conditions," *IEEE Transactions on vehicular technology*, vol. 55, no. 1, pp. 17–24, 2006.

[69] F. Seco, A. R. Jiménez, C. Prieto, J. Roa, and K. Koutsou, "A survey of mathematical methods for indoor localization," in *2009 IEEE International Symposium on Intelligent Signal Processing*. IEEE, 2009, pp. 9–14.

[70] F. D. Busse, J. P. How, and J. Simpson, "Demonstration of adaptive extended kalman filter for low-earth-orbit formation estimation using cdgps," *Navigation*, vol. 50, no. 2, pp. 79–93, 2003.

[71] A. Herschfelt and D. W. Bliss, "Spectrum management and advanced receiver techniques (smart): Joint radar-communications network performance," in *2018 IEEE Radar Conference (RadarConf18)*. IEEE, 2018, pp. 1078–1083.

[72] R. M. Gutierrez, A. Herschfelt, H. Yu, H. Lee, and D. W. Bliss, "Joint radar-communications system implementation using software defined radios: Feasibility and results," in *2017 51st Asilomar Conference on Signals, Systems, and Computers*. IEEE, 2017, pp. 1127–1132.

[73] B. Paul and D. W. Bliss, "Extending joint radar-communications bounds for fmcw radar with doppler estimation," in *2015 IEEE Radar Conference (RadarCon)*. IEEE, 2015, pp. 0089–0094.

[74] ——, "Constant information radar for dynamic shared spectrum access," in *2015 49th Asilomar Conference on Signals, Systems and Computers*. IEEE, 2015, pp. 1374–1378.

[75] ——, "The constant information radar," *Entropy*, vol. 18, no. 9, p. 338, 2016.

[76] D. W. Bliss, "Cooperative radar and communications signaling: The estimation and information theory odd couple," in *2014 IEEE Radar Conference*. IEEE, 2014, pp. 0050–0055.

[77] A. R. Chiriyath and D. W. Bliss, "Joint radar-communications performance bounds: Data versus estimation information rates," in *MILCOM 2015-2015 IEEE Military Communications Conference*. IEEE, 2015, pp. 1491–1496.

[78] B. Paul, A. R. Chiriyath, and D. W. Bliss, "Joint communications and radar performance bounds under continuous waveform optimization: The waveform awakens," in *2016 IEEE Radar Conference (RadarConf)*. IEEE, 2016, pp. 1–6.

[79] Y. Rong, A. R. Chiriyath, and D. W. Bliss, "Mimo radar and communications spectrum sharing: A multiple-access perspective," in *2018 IEEE 10th Sensor Array and Multichannel Signal Processing Workshop (SAM)*. IEEE, 2018, pp. 272–276.

[80] O. Ma, A. R. Chiriyath, A. Herschfelt, and D. W. Bliss, "Cooperative radar and communications coexistence using reinforcement learning," in *2018 52nd Asilomar Conference on Signals, Systems, and Computers*. IEEE, 2018, pp. 947–951.